Available online at www.sciencedirect.com
ScienceDirect
Geochimica et Cosmochimica Acta 70 (2006) 5552–5570
Geochimica
www.elsevier.com/locate/gca

Tracing end-member fluid sources in sub-surface iron mineralization and dolomitization along a proximal fault to the dead sea transform

Yigal Erel [a,*], Nora Listovsky [a], Alan Matthews [a], Shimon Ilani [b], Yoav Avni [b]

[a] *Institute of Earth Sciences, Hebrew University of Jerusalem, 91904 Jerusalem, Israel*
[b] *The Geological Survey of Israel, 30 Malkei Israel St., 95501 Jerusalem, Israel*

Received 12 April 2006; accepted in revised form 14 August 2006

Abstract

Shear faults in Upper Cretaceous limestones of the central Negev desert adjacent to the Dead Sea Transform (DST) feature extensive ferruginous mineralization and dolomitization. This has been related to topographically driven flow of metalliferous groundwaters through an underlying clastic (Nubian Sandstone) aquifer and rise of the fluids up the fault zones. The present study combines Pb and Sr isotope measurements with detailed sampling and petrography at the eastern end of the Paran fault (Menuha Ridge) in order to identify the types of groundwater and the sources of enriched elements in this regional-scale sedimentary mineralization. Ferroan and non-ferroan dolomitization along the Paran fault caused significant enrichment of several elements (Mg, Cu, Mn, Ni, V, Zn, Pb, and U) and $^{87}Sr/^{86}Sr$ values that are significantly higher than the Upper Cretaceous limestone country rock. The non-ferroan dolomite and the ferroan dolomite sampled at three sites along the Menuha Ridge have similar $^{87}Sr/^{86}Sr$ values 0.7076–0.7089, and 0.7077–0.7086, respectively. Additionally, there is a positive correlation between Mg-content of the dolomites and their $^{87}Sr/^{86}Sr$ values. The isotopic composition of Sr and Pb of dolomite corresponds to the mineralogical type identified in the mineralized rock (non-ferroan dolomite, simple-zoned ferroan dolomite, and complex-zoned ferroan dolomite). The $^{207}Pb/^{204}Pb$ and $^{206}Pb/^{204}Pb$ ratios of Fe oxides and dolomites from the three sites plot on a straight line, where the simple-zoned ferroan dolomite values are at the non-radiogenic end of the line and the complex-zoned ferroan dolomites at the radiogenic end. Both $^{206}Pb/^{204}Pb$ and $^{207}Pb/^{204}Pb$ ratios in dolomites and to a lesser degree in Fe-oxides suggest that a mixing between two end-members controls the behavior of Pb in the mineralization products along the Paran fault. Rather than a single fluid source, the study indicates that two types of metalliferous groundwaters were involved in the dolomitization and mineralization along the Paran fault. The first, and hitherto undocumented, fluid source is the Mg-rich Dead Sea Rift brine, migrating in the sub-surface before dolomitizing the carbonate bedrock. Migration of the brines took a deep path to the site of mineralization, with temperatures reaching 75 °C. Based on the geological history of the region, this probably took place in the Late Miocene–Early Pliocene interval. The second type of groundwater acquired its high solute concentrations from leaching igneous rocks and clastic sediments in the sub-surface, and infiltrated along the Paran fault, precipitating Fe-rich minerals and caused the first stage of dolomitization. This groundwater flowed at shallower depth than the DSR brines, and at lower temperatures ($T \leqslant 50$ °C). The study shows that sedimentary mineralization in faults adjacent to active transform fault zones may arise from the combination of several different fluid flow regimes.
© 2006 Elsevier Inc. All rights reserved.

1. Introduction

Reactive transport of groundwater is a major process in sedimentary basins, involving the movement of water and dissolved species that interact chemically with the host rock. Numerous studies have documented reactive

* Corresponding author. Fax: +972 2 5662581.
E-mail address: yerel@vms.huji.ac.il (Y. Erel).

0016-7037/$ - see front matter © 2006 Elsevier Inc. All rights reserved.
doi:10.1016/j.gca.2006.08.019

transport that caused rock diagenesis and hydrothermal mineralization (e.g., Steefel and Van Cappellen, 1998, and references therein). Both Sr and Pb isotopes have been used extensively in studying the sources, migration paths and timing of large scale sub-surface groundwater flow and mineralization phenomena (e.g., Heyl et al., 1966, 1974; Burke et al., 1982; Hess et al., 1986; Avigour et al., 1990; Banner, 1995). Of significant importance is the behavior of metal-rich waters that are involved in the precipitation of economical ore deposits (e.g., Ohle, 1980; Bethke, 1986; Sverjensky, 1986; Bethke and Marshak, 1990; Garven et al., 1993). The Mississippi Valley type ores (MVT) are prime examples of such deposits. Numerous studies have established that long-range migration of brines involved in the formation of MVT deposits was driven by recharge from topographically high areas towards the margins of basins, fault zones, and anticlines, where they rose and encountered conditions that allowed ore–mineral precipitation (e.g., Ohle, 1980; Bethke, 1986; Sverjensky, 1986; Garven et al., 1993; Garven, 1995; Appold and Garven, 1999).

Iron mineralization (ferruginous lenses and iron oxide vein stockworks) and iron-bearing (ferroan) dolomitization in Upper Cretaceous carbonates along major E-W trending faults in the Negev, southern Israel (Figs. 1 and 2) have been studied for their economic potential and paragenesis since the 1950s (Dessau, 1951; Hanreck, 1952; Solomonica, 1952; Bentor, 1953; Shraga, 1971; Ilani et al., 1985, 1988; Ilani, 1989; Avigour et al., 1992). Among the mechanisms proposed for this mineralization, the most strongly favored is topographically driven northward-directed groundwater flow through the underlying Jurassic–Lower Cretaceous sandstone, from recharge areas in the Sinai Mountains (Issar et al., 1972; Ilani et al., 1985, 1988, 1989; Avigour et al., 1992). Leaching of metals from the underlying clastic sandstone (Nubian) aquifer was considered to be a major source of most metallic elements, with the important exception of magnesium, which was suggested to have originated in brines of Sinai and Southern Israel (Ilani et al., 1988). Regional-scale faulting (the Negev Shear zone) related to the Dead Sea Transform, which initiated in the Miocene, facilitated the rise of the over pressured solutions along fault lines and allowed the dolomitization and mineralization of the overlying carbonate rocks (Bartov, 1974; Ilani et al., 1988). The sedimentary basinal setting of the mineralization was confirmed by oxygen isotope studies of ferruginous lenses, which showed that they formed at temperatures of 50 ± 10 °C (Grosz et al., 2006).

The proximity to the Dead Sea Transform, however, raises the possibility of an alternative origin for the Mg-rich solutions needed for dolomitization. Geochemical studies of groundwater wells and theoretical calculations have both suggested that density driven migration of saline Mg-rich brines from the Dead Sea Rift into adjacent carbonate rocks could have resulted in dolomitization (Starinsky, 1974; Stanislavsky and Gvirtzman, 1999). The need to examine this alternative is reinforced by detailed petrographic and oxygen isotope studies of dolomites (Grosz et al., 2006, see next section), which suggest that at least two fluid flow patterns are involved in the dolomitization: an earlier one characterized by $T \leqslant 50$ °C and a later one characterized by $T \geqslant 50$ °C and lower $\delta^{18}O$ groundwater. Pb and Sr isotopes are ideal tools for elucidating the origin of the fluids involved in the iron mineralization and dolomitization, since they monitor elements such as Fe and Mg, respectively. The aim of this study was to determine the sources of the iron mineralization and dolomitization using Pb and Sr isotopic ratios. We show that a substantial part of the mineralization and dolomitization can be related to a unique sequence of events corresponding to when southward migrating brines in the Dead Sea rift were incorporated in a westward-directed topographically driven groundwater system.

2. Geological and petrographical setting

2.1. Study area

The Negev Shear zone consists of a series of shear faults that are offset by the Dead Transform (DST) (Fig. 1). The exposures of iron mineralization and ferroan dolomitization studied in this work are located along the eastern part (the Menuha ridge segment) of one of the major faults—the Paran fault—and are hosted by the Middle to Late Cretaceous (Late Albian to Coniacian) carbonate sequences (Judea Group: Shraga, 1971; Bartov et al., 1972; Ilani, 1989; Sakal, 1998) (Fig. 1).

The carbonatic Judea Group is a part of the sedimentary platform cover overlying the Precambrian Arabo–Nubian Massif. The Judea Group carbonate rocks that are dolomitized and mineralized at Menuha Ridge (Figs. 1 and 2) mainly belong to the Cenomanian *Tamar* Formation, dominated by limestones, the Lower Turonian *Ora* Formation that consists of limestone and calcareous shales, and the Upper Turonian *Gerofit* Formation that consists mainly of limestone (1:200,000 map of Israel, sheet 4; Sneh et al., 1998). The Judea Group rocks in the Menuha Ridge region are underlain by a sequence of predominantly continental sandstones (“Nubian sandstone”) of the Hatira Formation of the Early Cretaceous Kurnub Group and of the Cambrian Yam Suf Group. Permian, Triassic, and Jurassic sediments, well developed farther south, are probably absent, having been truncated by Early Cretaceous erosion (Garfunkel, 1988). In the study area, the Cambrian sediments overlie Precambrian arkoses (Zenifim Formation) that overlie an igneous–metamorphic basement, composed mainly of metamorphic and intermediate and basic igneous rocks (Segev et al., 1999). Although the basement rocks are not exposed in the Paran region, their sub-surface composition can be deduced from the rock assemblage exposed in the Timna area, some 50–60 km to the south (Beyth, 1987; Beyth et al., 1994). The basement rocks were shaped by the Late Proterozoic Pan-African orogeny that is widely exposed farther south (the Arabo–Nubian shield) and is the

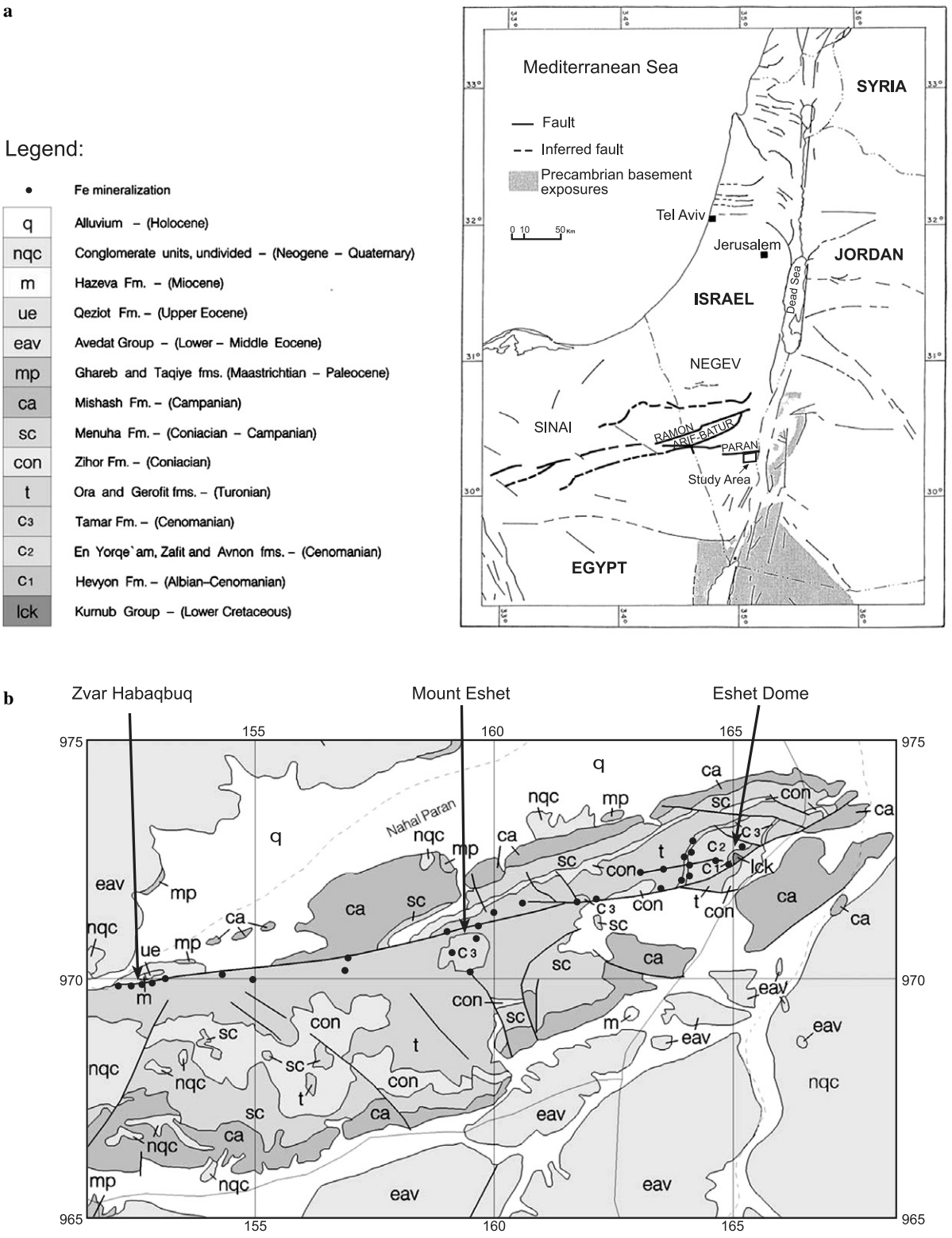

Fig. 1. (a) Schematic map of Israel, including major tectonic features (the major faults in the central Negev shear zone are highlighted in bold), and showing the Menuha Ridge study area. Seismic profiling studies have shown that the Paran Fault at Menuha Ridge is a steep southward-dipping oblique dextral slip-strike system. (Dvory, 2002). (b) The geology of the study area showing sites of the ore occurrences along the Menuha Ridge area of the Paran Fault (after Sakal, 1998 and Sneh et al., 1998). Sites of iron mineralization are indicated by dots. The sites studied in this work are Zvar Habaqbuq (ZH), Mt. Eshet (ME), and the Eshet Dome (ED).

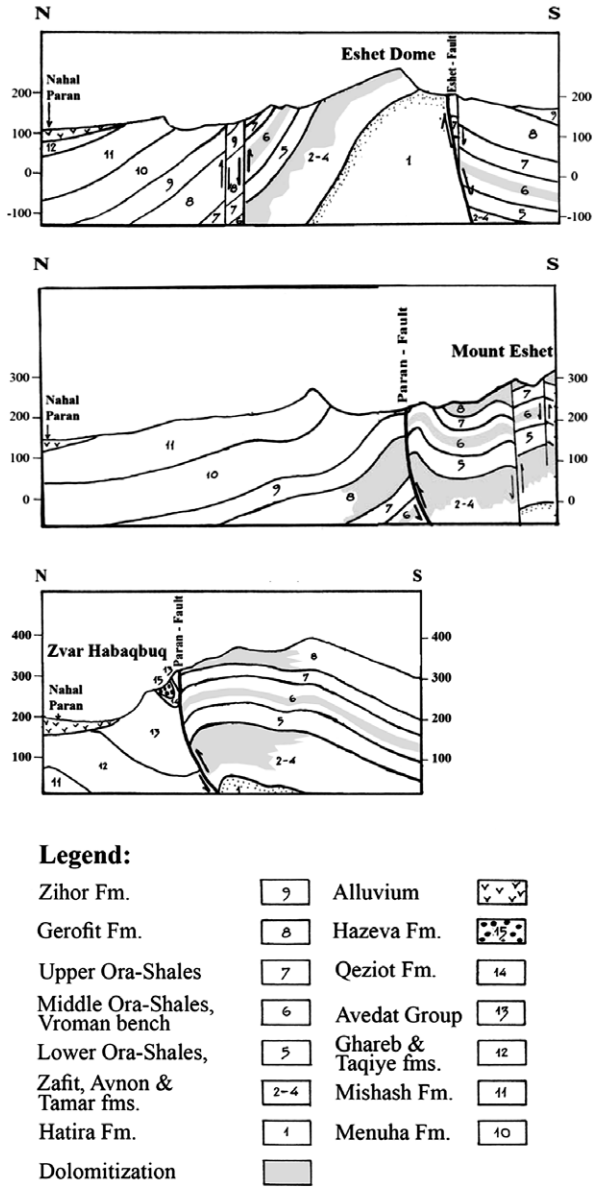

Fig. 2. North-south schematic cross-sections though Zvar Habaqbuq, Mt. Eshet and Eshet dome, showing the relations of the dolomitization to the stratigraphic units (modified after Sakal, 1998).

main sediment source for the Nubian sequences (Weissbrod and Nachmias, 1986; Garfunkel, 1999).

The Menuha Ridge consists of a nearly E-W trending irregular anticlinal structure whose southern flank is displaced by the Paran Fault (Sakal, 1998). Folding and differential fault movements that produced the exposed structure occurred intermittently from the Senonian to the Miocene. Along the eastern part of Menuha Ridge the block south of the fault is downthrown, and the dolomitized Cenomanian–Turonian rocks are exposed on the north side. Along the western part of the Menuha Ridge, the northern block is downthrown and the dolomitized and iron mineralized Cretaceous rocks are exposed on the south side of the fault, and juxtaposed against non-mineralized Eocene beds (Avedat Group). The locations and simplified cross-sections of iron mineralization and dolomitization exposures studied in this work are shown in Figs. 1 and 2, respectively: (1) Zvar Habaqbuq (ZH) (literal translation, the Bottleneck) in the west of the area; (2) Mount Eshet (ME) in the central part where the Cretaceous sequences are exposed on both sides of the Paran fault and (3) Eshet Dome (ED) in the east of the area.

2.2. Field setting and petrography of dolomites

The iron mineralization dominantly occurs as discontinuous lenses in or adjacent to the fault zone and as vein stockworks cutting the host rock. The dolomite is characterized by a deep-red colouration, which frequently stands out against the pale-coloured limestone; consequently beds can be traced easily along strike (Grosz et al., 2006). Dolomitization at Zvar Habaqbuq (ZH) in the west of the area occurs in the *Ora* and *Gerofit* formations exposed on the south side of the Paran fault (Figs. 1 and 2), whereas at Eshet Dome (ED) it dominantly occurs in the *Tamar* Formation, north of the fault (Fig. 2) (Listovsky, 2004).

The main *Ora* Formation dolomitized layer at the sampled localities is a *ca* 5 m thick distinct horizon known as the Vroman Bank, overlain by marls. At Mt. Eshet (ME) the dolomitized portion of this horizon can be followed up to about 1500 m from the fault, whereas at ZB the steep topography only allowed it to be sampled up to 170 m from the fault. A dense dark brown ferroan dolomite horizon also characterizes the upper part of the *Tamar* Formation underlying the *Ora* Formation at ME (Fig. 2). This dolomitized bed is at least 30 m thick and terminates approximately 600 m away from the fault where it passes into unaltered limestone. The ED locality exposes ferroan dolomite that forms the uppermost part of the *Tamar* Formation. This dolomite can be followed approximately 1000 m from the fault where it terminates and gives way to unaltered biomicritic limestone. Grosz et al. (2006) showed that the dolomites can be classified into three textural and mineralogical types.

1. *Non-ferroan dolomites and dedolomites (NFD)*. These rocks are characterized by the presence of calcite in the cores of dolomite grains and the absence of iron-bearing phases or Fe^{2+} in the calcite cores and the dolomite rims. These rocks are exposed in The Upper Turonian *Gerofit* formation rocks at ZH.
2. *Simple-zoned ferroan dolomites (SZFD)*. The ferroan dolomites exhibit a zonal structure characterized by iron-rich cores. The dolomite cores consist of arrays of very small iron oxide crystals preserving the characteristic rhombohedral crystal form. These rhombohedral cores are mantled by transparent dolomite. The inference of this zonal structure is that the initial dolomite was ferroan, but fluid conditions subsequently changed to allow alteration of the dolomite and formation of iron (III) oxides, which pseudomorphically preserved the

rhombohedral shape of the original dolomite. These are found in the Turonian *Ora* (Vroman Bank) Formation at ZH and the *Gerofit* Fomation at ME.

3. *Complex-zoned ferroan dolomites (CZFD)*. These rocks resemble those of the simple-zoned dolomites, except that the initial zoning pattern is repeated. The ferroan dolomite contains rhombohedral cores with hematite (as in simple-zoned dolomites) that are successively surrounded by ferroan dolomite and hematite-rich rims that mimic the shape of the cores. These textures indicate more prolonged exposure to Fe and Mg-enriched solutions and redox cycling compared to the relatively simple zoning dolomites (Grosz et al., 2006). These rocks are found in the Cenomanian *Tamar* Formation rocks at ME and ED and Vroman Bank at ME.

3. Experimental methods

Sampling was carried out based on stratigraphic and geographic location. Hence, ferroan dolomite, dolomite, and Fe-oxides samples were collected from all the exposed formations in each of the three sites. At each site samples were taken at various distances from the Paran fault zone (see also Grosz et al., 2006). Unaltered bedrock was sampled from each sampled formation for comparison (Table 1). A total of more than 100 samples were collected, including 55 dolomites, 40 Fe-oxides, and four unaltered bedrock samples. In addition, we collected rock samples which should represent the composition of near-by igneous bodies (Bentor and Vroman, 1954). This includes five rock samples from the mafic Ashosh plug and four rock samples from the syenitic Ramon intrusion (Tables 1 and 2). We also dissolved and analyzed six samples of dolomite collected in a previous study in the Judean desert near the Dead Sea (Table 2; Doron, 2000). Seven Kurnub groundwater samples (provided by S. Henig, Ben Gurion University of the Negev) were also included in this study.

Prior to dissolution all samples were crushed, sieved, and homogenized in order to obtain representative samples. The dissolution and the preparation of samples for analysis were conducted in a clean laboratory using distilled acids and water in order to minimize Pb and Sr pollution from anthropogenic (Pb) and natural (Sr) atmospheric dust. Dolomite samples were dissolved in concentrated HCl. Fe-oxides samples were dissolved in two steps. First, secondary calcite was dissolved with a combination of Na-acetate and acetic acid at pH 5.0, and then the residue was dissolved in heated (80 °C) concentrated HCl. Known volumes of acidified Kurnub groundwater samples were evaporated down and then dissolved in 10 ml dilute HNO_3.

Concentrations of Fe, Ca, and Mg were measured with a Perkin-Elmer PC-5100 ZL Atomic Absorption spectrometer using Merck standard solutions. Sr, Ti, Mn, and Ba concentrations were determined with a Perkin-Elmer Optima 3000 ICP-OES, and Co, Cr, Cs, Cu, Ni, Rb, V, Zn, Pb, U, and Th concentrations with an ICP-MS (Perkin-Elmer SCIEX, CDR II). The precision of the measurements was less than 15% for the AA, and less than 10% for both the ICP-OES and ICP-MS.

Strontium and Pb were separated for isotopic measurements using ion exchange columns (Eichrom Sr-Spec (50–100 mesh) and Dowex 1X8, 100–200 mesh ion exchange resins, respectively). Isotopic measurements were conducted with a MC-ICP-MS (Nu Instruments). Blank levels were checked regularly and never exceeded 1% of the samples. Mass fractionation was closely monitored by frequent analysis of NIST standards under identical running conditions as samples. The NIST 981 standard was used for Pb isotope calibration and had long-term mean values of: $^{206}Pb/^{204}Pb = 16.93 \pm 0.01$, $^{207}Pb/^{204}Pb = 15.48 \pm 0.01$, $^{208}Pb/^{204}Pb = 36.68 \pm 0.02$ (1σ, $n = 21$) (Listovsky, 2004). Mass fractionation corrections for Pb in both samples and NIST-981 standard were based on a $^{205}Tl/^{203}Tl$ isotopic ratio of 2.3875 after adding a Tl solution (50 ppb) to both the NIST 981 standard and to the samples. $^{87}Sr/^{86}Sr$ ratios were corrected for mass fractionation to $^{86}Sr/^{84}Sr = 0.1194$. Analyses of NIST SRM 987 had a mean value of 0.71027 ± 0.00004 (1σ, $n = 29$). Oxygen isotope compositions used in this study are taken from Grosz et al. (2006) and are reported relative to the SMOW scale.

4. Results

The ferroan and non-ferroan dolomitization along the Paran fault caused significant enrichment of several elements relative to the limestone country rock (Table 1). For example, Mg concentrations increased from less than a percent to 10% in the epigenetic dolomite and Fe concentrations increased from a few hundred ppm to 40–50% in the Fe-oxides within the dolomite (Table 1). The concentrations of other elements such as Cu, Mn, Ni, V, Zn, Pb, and U increased mostly in the ferroan dolomites, but also in the non-ferroan dolomites (Table 1). The enrichments of these elements were also associated with large differences in the isotopic composition of Sr between the primary limestone and the products of the ferroan dolomitization (Table 2).

$^{87}Sr/^{86}Sr$ values have similar ranges in the non-ferroan dolomite and in the ferroan dolomite (0.7076–0.7089, and 0.7077–0.7086, respectively; Table 2). In both sample types, $^{87}Sr/^{86}Sr$ values in the westernmost site furthest from the Dead Sea Rift (ZH) are the lowest (0.7077–0.7083; Table 2). In addition, there is a positive correlation between Mg-content of the dolomites and their $^{87}Sr/^{86}Sr$ values (Fig. 3; Table 2). In general, complex-zoned ferroan dolomites and Fe-oxides have the highest $^{87}Sr/^{86}Sr$ values and simple-zoned ferroan dolomites and Fe-oxides have the lowest (Fig. 3). Nevertheless, the isotopic composition of Sr does not indicate a simple mixing between two end-members (i.e., no straight line relationship in a $^{87}Sr/^{86}Sr$ vs. 1/[Sr] plot), for reasons that will be discussed later.

Table 1
Chemical composition of sampled rocks

Location	Texture, form	Sample	Ca%	Mg%	Ba	Co	Cr	Cs	Cu	Fe	Mn	Ni	Pb	Rb	Sr	Ti	Th	U	V	Zn
Dolomite																				
ZH	SZFD, Ora	00/05	19	10.5	6	0.8		0.008	1.09	9600	1810	69	2.5	0.1	76	bdl	0.032	0.32	7.8	29
ZH	SZFD, Ora	00/06	23	6.4	—	—	—	—	—	6800	—	—	—	—	—	—	—	—	—	—
ZH	SZFD, Ora	00/07	27	12.4	6	0.9	9.4	0.030	bdl	3400	670	1.9	6.2	0.3	109	8.8	0.143	0.47	8.2	12
ZH	SZFD, Ora	00/08	31	1.91	—	—	—	—	—	700	—	—	—	—	—	—	—	—	—	—
ZH	SZFD, Ora	00/09	18	11	—	—	—	—	—	16,400	—	—	—	—	—	—	—	—	—	—
ZH	SZFD, Ora	00/10	17	9.3	25	1.2	bdl	0.027	1.38	14,000	2700	140	5.7	0.4	88	bdl	0.148	0.32	9.8	180
ZH	SZFD, Ora	00/11	22	9.1	—	—	—	—	—	42,000	—	—	—	—	—	—	—	—	—	—
ZH	SZFD, Ora	00/12	20	10.3	—	—	—	—	—	18,900	—	—	—	—	—	—	—	—	—	—
ZH	SZFD, Ora	00/13	23	11.7	—	—	—	—	—	23,000	—	—	—	—	—	—	—	—	—	—
ZH	SZFD, Ora	00/15	25	10.4	—	—	—	—	—	330	—	—	—	—	—	—	—	—	—	—
ZH	NFD, Grofit	00/25	22	3.8	—	—	—	—	—	1190	—	—	—	—	—	—	—	—	—	—
ZH	NFD, Grofit	03/113	21	11.6	35	0.9	bdl	0.017	0.98	11,000	1150	111	16.1	0.3	87	bdl	0.079	1.22	73	86
ZH	NFD, Grofit	03/114	24	13.4	—	—	—	—	—	6300	—	—	—	—	—	—	—	—	—	—
ZH	NFD, Grofit	03\115	31	12.8	13.4	0.57	bdl	0.013	0.32	1400	290	11.4	0.70	0.169	121	bdl	0.056	0.54	15.2	11.5
ZH	NFD, Grofit	03\117	24	13.0	21	0.69	bdl	0.015	0.65	220	350	4.0	0.196	0.20	61	bdl	0.076	0.52	14.3	6.7
Mt. Eshet	SZFD, Grofit	01\58	29	12	28	0.75	11	0.045	n.d.	25,000	340	1.9	0.49	0.5	46	13.1	0.139	0.52	5.6	12
Mt. Eshet	SZFD, Grofit	01\64	20	9.3	27	0.56	13	0.015	0.37	10,300	1500	2.1	8.6	0.1	77	8.3	0.056	2.4	7.5	22
Mt. Eshet	CZFD, Tamar	01\77	19	11.3	—	—	—	—	—	17,700	—	—	—	—	—	—	—	—	—	—
Mt. Eshet	CZFD, Tamar	02\80	22	9.8	32	1.21	bdl	0.100	5.5	7300	3800	65	0.56	1.6	97	bdl	0.141	1.93	25	9.4
Mt. Eshet	CZFD, Tamar	02\81	20	13	32	1	bdl	0.183	2.1	5200	2300	36	0.54	2.9	—	bdl	0.166	0.8	11.7	4
Mt. Eshet	CZFD, Tamar	02\82	22	12	43000	1660	bdl	91.000	2100	7500	4E+05	58,000	930	1420	69	bdl	380	640	12,500	4800
Mt. Eshet	CZFD, Ora	02\83	19	11.3	27	1.54	bdl	0.110	3.3	7900	5100	68	0.65	1.5	68	bdl	0.85	2.1	22	4.5
Mt. Eshet	CZFD, Ora	02\84	21	11.2	—	—	—	—	—	7300	—	—	—	—	—	—	—	—	—	—
Mt. Eshet	CZFD, Ora	02\86	21	11.6	31	0.66	bdl	0.050	1.62	10,400	4400	77	0.27	0.8	57	bdl	0.068	1.75	14.9	5.8
Mt. Eshet	CZFD, Ora	02\87	20	5.1	—	—	—	—	—	23,000	—	—	—	—	—	—	—	—	—	—
Mt. Eshet	CZFD, Ora	02\91	22	12.2	37	0.62	bdl	0.023	60	2500	660	24	5.8	0.4	45	bdl	0.1	0.6	17.3	22
Mt. Eshet	CZFD, Ora	02\92	19	8.8	105	1.41	bdl	0.035	1.2	72,000	0230	470	23	0.4	62	bdl	0.23	2.8	19.4	460
Mt. Eshet	CZFD, Ora	02\95	23	12.3	18.5	0.63	bdl	0.031	0.51	9700	.490	69	8.4	0.4	90	bdl	0.169	0.65	11.7	27
Mt. Eshet	CZFD, Tamar	02\98	5	0.19	—	—	—	—	—	14,500	—	—	—	—	—	—	—	—	—	—
Mt. Eshet	SZFD, Grofit	02\100	24	11.4	—	—	—	—	—	14,500	—	—	—	—	—	—	—	—	—	—
Mt. Eshet	SZFD, Grofit	02\101	26	11.3	—	—	—	—	—	14,900	—	—	—	—	—	—	—	—	—	—
Mt. Eshet	SZFD, Grofit	02\102	26	12	—	—	—	—	—	13,800	—	—	—	—	—	—	—	—	—	—
Mt. Eshet	SZFD, Grofit	02\104	20	9.8	—	—	—	—	—	38,000	—	—	—	—	—	—	—	—	—	—
Mt. Eshet	SZFD, Grofit	02\106	20	11.7	—	—	—	—	—	7200	—	—	—	—	—	—	—	—	—	—
Mt. Eshet	CZFD, Tamar	03\122	25	11.4	—	—	—	—	—	11,500	—	—	—	—	—	—	—	—	—	—
Mt. Eshet	CZFD, Tamar	03\123	25	11.4	—	—	—	—	—	9800	—	—	—	—	—	—	—	—	—	—
Mt. Eshet	CZFD, Tamar	03\124	25	12	—	—	—	—	—	9600	—	—	—	—	—	—	—	—	—	—
Mt. Eshet	CZFD, Tamar	03\125	24	10.6	—	—	—	—	—	13,400	—	—	—	—	—	—	—	—	—	—
Mt. Eshet	CZFD, Tamar	03\126	27	11.1	—	—	—	—	—	2200	—	—	—	—	—	—	—	—	—	—
Eshet Dome	Ora	00/28	17	9.9	11.2	0.81	bdl	0.006	1.92	580	260	10.5	0.119	0.094	62	bdl	0.037	1.45	20	2.7
Eshet Dome	CZFD, Tamar	00/34	23	10.5	45	bdl	bdl	0.023	0.9	22,000	9000	3	0.2	0.3	390	12.5	0.07	1.5	13	20
Eshet Dome	CZFD, Tamar	00/35	20	12.5	—	—	—	—	—	9400	—	—	—	—	—	—	—	—	—	—
Eshet Dome	CZFD, Tamar	00/38	23	5	—	—	—	—	—	24,000	—	—	—	—	—	—	—	—	—	—
Eshet Dome	CZFD, Tamar	00/40	24	5.9	—	—	—	—	—	6900	—	—	—	—	—	—	—	—	—	—
Eshet Dome	CZFD, Tamar	00/41	26	11.1	49	0.75	10.12	0.015	0.75	30,000	2900	0.75	1.87	0.12	69	8.2	0.071	1.61	15	490
Eshet Dome	CZFD, Tamar	00/42	21	5.7	—	—	—	—	—	6300	—	—	—	—	—	—	—	—	—	—
Eshet Dome	CZFD, Tamar	00/43	23	11	73	1	bdl	0.036	0.9	19,700	2000		6.5	0.33	310	23	0.18	2.8	11	57

(*continued on next page*)

Table 1 (*continued*)

Location	Texture, form	Sample	Ca%	Mg%	Ba	Co	Cr	Cs	Cu	Fe	Mn	Ni	Pb	Rb	Sr	Ti	Th	U	V	Zn
Eshet Dome	CZFD, Ora	03/131	26	10.5	33	0.89	bdl	0.009	3.1	11,000	1520	71	1.42	0.134	260	bdl	0.058	1.52	25	14.3
Eshet Dome	CZFD, Ora	03/132	29	9.7	33	1.83	bdl	0.017	7.8	3800	680	37	0.86	0.29	94	bdl	0.093	1.59	27	8
Eshet Dome	CZFD, Ora	03/134	23	12.1	28	0.92	bdl	0.010	3.1	2300	940	20	0.38	0.147	96	bdl	0.064	1.77	21	5.5
Eshet Dome	CZFD, Ora	03/135	24	10.8	21	1.34	bdl	0.021	4.6	2100	1000	32	1.9	0.27	75	bdl	0.114	1.69	33	19.6
Eshet Dome	CZFD, Ora	03/136	25	12.3	21	0.8	bdl	0.014	2.7	3800	1770	49	0.61	0.189	66	bdl	0.074	1.52	23	23
Eshet Dome	CZFD, Tamar	03/146	26	13.3	—	—	—	—	—	7100	—	—	—	—	—	—	—	—	—	—
Eshet Dome	CZFD, Tamar	03/147	24	11.3	—	—	—	—	—	7700	—	—	—	—	—	—	—	—	—	—
Eshet Dome	CZFD, Tamar	03/148	23	11.5	47	1.52	bdl	0.008	2.5	31,000	6900	210	8.7	0.16	84	bdl	0.047	1.81	34	31
Eshet Dome	CZFD, Tamar	03/149	26	10.6	108	1.95	bdl	0.008	1.19	34,000	2300	220	2.9	0.115	103	bdl	0.05	2	26	20
Eshet Dome	CZFD, Tamar	03/156	23	11.3	77	0.97	bdl	0.008	1.44	25,000	4600	171	2.2	0.144	83	bdl	0.043	1.83	26	25
Eshet Dome	CZFD, Tamar	03/157	25	11.1	—	—	—	—	—	7900	—	—	—	—	—	—	—	—	—	—
Eshet Dome	CZFD, Tamar	03/158	—	—	—	—	—	—	—	7100	—	—	—	—	—	—	—	—	—	—
Eshet Dome	CZFD, Tamar	03/159	26	12.2	33	0.71	bdl	0.003	1.49	6200	1510	43	1.72	0.089	92	bdl	0.036	2.1	21	65
Eshet Dome	CZFD, Tamar	03/160	—	—	—	—	—	—	—	5500	—	—	—	—	—	—	—	—	—	—
Eshet Dome	CZFD, Tamar	03/161	18	8.2	—	—	—	—	—	9000	—	—	—	—	—	—	—	—	—	—
Location	Texture form	Sample	Ca	Mg	Ba	Co	Cr	Cs	Cu	Fe%	Mn	Ni	Pb	Rb	Sr	Ti	Th	U	V	Zn
Fe-oxides																				
ZH	Ora	00\01	720	1430	75	bdl	7.5	3.000	11.2	69	2E+05	15.0	290	0.086	75	67	0.30	0.64	34	1570
ZH	Ora	00\02	1000	800	250	bdl	20.0	0.050	8.0	25	170	bdl	135	bdl	35	60	0.20	1.50	bdl	400
ZH	Ora	00\04	bdl	1460	47	bdl	5.6	2.100	15.0	69	56000	11.2	161	0.079	24	41	0.187	0.60	bdl	2600
ZH	Ora	00\16	350	710	1240	bdl	15.0	1.690	11.2	52	bdl	bdl	56	0.056	139	520	0.15	0.26	41	75
ZH	Ora	00\17	197	78	—	—	—	—	—	2.9	—	—	—	—	—	—	—	—	—	—
ZH	Ora	00\18	bdl	bdl	—	—	—	—	—	10.5	—	—	—	—	—	—	—	—	—	—
ZH	Ora	00\19	bdl	730	67	bdl	7.5	2.100	11.2	49	60000	11.2	270	0.052	30	188	0.37	0.28	15	990
ZH	Ora	00\20	860	1090	490	2.1	bdl	0.030	10.2	37	1450	2700	198	0.41	77	bdl	0.15	2.6	67	1710
ZH	Ora	00\22	bdl	100	25	bdl	bdl	0.040	bdl	0.23	10	bdl	11.0	bdl	8	10	0.07	0.04	bdl	100
ZH	Ora	00\47	1420	1770	410	bdl	15.0	2.200	15.0	59	37000	16.9	520	0.127	82	360	0.37	0.56	34	1500
ZH	Ora	01\69	1030	3100	560	bdl	11.2	1.690	11.2	51	9400	7.5	182	0.037	135	300	0.075	1.01	15	470
ZH	Ora	01\70	1500	2500	250	bdl	10	0.040	5.0	44	1750	25	290	bdl	80	100	0.40	1.00	30	2200
ZH	Ora	01\71	bdl	113000	310	1.32	bdl	0.010	8.9	50	1160	3300	109	0.22	114	bdl	0.33	0.35	86	1990
ZH	Ora	01\75	bdl	710	51	bdl	15.0	1.870	16.9	79	86000	11.2	230	bdl	22	18.8	0.30	1.01	11.2	1160
ZH	Ora	01\76	bdl	720	37	bdl	7.5	1.690	15.0	55	15000	7.5	174	bdl	11	64	0.30	2.8	bdl	520
ZH	Ora	03\118	36000	870	—	—	—	—	—	39	—	—	—	—	—	—	—	—	—	—
ZH	Ora	03\119	47000	530	—		—	—	—	24	—	—	—	—	—	—	—	—	—	—
ZH	Ora	03\120	29000	720	—	—	—	—	—	22	—	—	—	—	—	—	—	—	—	—
ZH	Ora	03\121	33000	bdl	—	—	—	—	—	20	—	—	—	—	—	—	—	—	—	—
Mt. Eshet	Tamar	00\49	670	3600	72	0.2	bdl	bdl	3.5	42	116	3100	1.84	0.043	33	bdl	0.09	2.1	70	24
Mt. Eshet	Tamar	01\50	500	1100	95	bdl	bdl	0.060	1	53	300	25	1.5	0.2	20	20	0.2	1.7	bdl	130
Mt. Eshet	Tamar	01\51	500	580	21	0.34	bdl	0.018	1.82	49	330	3300	0.43	0.036	15	bdl	0.04	4.1	64	14.6
Mt. Eshet	Tamar	01\52	1000	1800	185	bdl	10	0.050	2	58	250	30	1.3	bdl	40	20	0.1	3.5	bdl	150
Mt. Eshet	Tamar	01\54	—	—	80	1.68	bdl	0.040	6.4		1730	3100	4.4	0.6	178	bdl	0.28	13.8	77	32
Mt. Eshet	Tamar	01\55	10900	4000	360	1.12	13.13	0.049	11.2	58	2E+05	15	5.6	0.37	138	18.7	0.41	7.9	22	146
Mt. Eshet	Tamar	01\56	2900	4900	520	3.00	bdl	0.080	11.6	56	1240	3300	6.3	0.76	310	bdl	0.31	8.9	128	360
Mt. Eshet	Tamar	01\57	1300	2400	600	0.67	bdl	0.011	4.2	49	410	3200	1.9	0.117	161	bdl	0.11	4.1	75	67
Mt. Eshet	Grofit	01\61	42000	1430	93	0.34	bdl	0.012	23	42	330	2800	1.73	0.139	121	bdl	0.24	4.9	500	76
Mt. Eshet	Grofit	O1\65	740	3300	490	bdl	30	0.034	13.1	75	64000	22	250	0.169	75	150	0.71	10.1	187	250
Mt. Eshet	Grofit	01\66	4700	7100	—	—	—	—	—	53	—	—	—	—	—	—	—	—	—	—

Mt. Eshet	Grofit	01\67	13900	2500	142	bdl	41	0.022	11.2	56	49000	18.7	120	0.083	34	13.1	0.79	21	60	220
Mt. Eshet	Grofit	02\103	196000	3400	430	1.91	bdl	0.094	3.7	23	1270	1410	53	0.91	101	bdl	0.26	4.4	115	610
Mt. Eshet	Grofit	02\105	53000	4800	530	1.93	bdl	0.051	4.6	40	860	2600	60	0.6	105		0.35	14.1	188	560
Eshet Dome	Tamar	00/32	290	5100	—	—	—	—	—	38	—	—	—	—	—	—	—	—	—	—
Eshet Dome	Tamar	00/33	18500	1590	—	—	—	—	—	40	—	—	—	—	—	—	—	—	—	—
Eshet Dome	Tamar	00/36	2500	3000	1200	4.0	15.00	0.130	10.0	49	1700	40	7.0	1.00	260	45	0.5	5.0	45	340
Eshet Dome	Tamar	00/37	1000	1500	1650	bdl	25	0.050	3.0	48	110	35	1.50	bdl	40	110	0.3	10.0		75
Eshet Dome	Tamar	00/39	2200	1470	118	bdl	9.4	0.019	15.0	70	3700	13.1	9.4	0.052	30	22	0.075	2.0	52	75
Eshet Dome	Tamar	03/162	760	5400						40										
Eshet Dome	Tamar	03/163	880	1650	420	0.54	bdl	0.030	2.3	55	1930	3500	1.05	0.53	94	bdl	0.096	2.0	64	29
Eshet Dome	Tamar	03/164	42	1180	—	—	—	—	—	42	—	—	—	—	—	—	—	—	—	—
Eshet Dome	Tamar	03/165	517	790	—	—	—	—	—	53	—	—	—	—	—	—	—	—	—	—
Eshet Dome	Tamar	03/166	1590	3200	550	1.88	bdl	0.051	6.0	57	1200	3200	3.4	0.8	157	bdl	0.26	3.2	106	63
Eshet Dome	Tamar	03/167	1840	2000	820	1.30	bdl	0.007	5.0	58	690	3400	5.8	0.23	220	bdl	0.25	4.4	90	38
Eshet Dome	Tamar	03/168	590	1210	—	—	—	—	—	58	—	—	—	—	—	—	—	—	—	—
Eshet Dome	Tamar	03/169	1250	1570	—	—		—	—	49	—	—	—	—	—	—	—	—	—	—
Eshet Dome	Tamar	03/170	740	1750	—	—	—	—	—	53	—	—	—	—	—	—	—	—	—	—
Location	Texture form	Sample	Ca%	Mg%	Ba	Co	Cr	Cs	Cu	Fe	Mn	Ni	Pb	Rb	Sr	Ti	Th	U	V	Zn
Host rock limestone and digenetic dolomite																				
ZH	Grofit	00/24	45	1.93	13.3	0.9	bdl	0.018	0.76	1060	217	15	0.36	0.3	160	bdl	0.089	0.7	12.5	4.8
Eshet Dome	Tamar	00\26	36	0.105	42	1.00	1.00	0.008	0.90	310	260	2.00	0.20	0.04	140	10.0	0.05	1.00	7.0	18.5
Eshet Dome	Tamar	00\30	36	0.27	27	1.00	bdl	0.012	0.90	1300	1000	2.00	0.50	0.05	240	10.0	0.10	3.4	16.5	20
Mt. Eshet	Grofit	03\128	57	0.23	13.7	0.74	bdl	0.004	0.55	410	220	6.5	0.123	0.07	350	bdl	0.024	1.74	17.6	2.0
Govai Mnt.	Ora	03\130	33	11	17	1.36	bdl	0.032	0.90	2800	230	23	0.38	0.34	171	bdl	0.063	0.27	9.9	5.0
			Ca%	Mg%	Ba*	Co*	Cr	Cs*	Cu*	Fe%	Mn*	Ni*	Pb*	Rb*	Sr*	Ti	Th*	U*	V*	Zn*
Ashosh plug																				
		Ash171	7.3	4.1	300	37	—	0.116	33	12	1620	580	3.0	12.3	320	—	2.0	0.46	450	360
		Ash172	5.7	3.3	280	38	—	0.093	24	26	1770	560	2.9	8.3	300	—	1.71	0.39	440	330
		Ash173	5.7	4.8	280	38	—	0.179	39	26	1680	570	3.1	15.1	310	—	2.0	0.45	410	350
		Ash174	7.0	3.9	290	36	—	0.136	23	15	1500	540	2.5	11.9	290	—	1.55	0.38	430	340
		Ash175	8.6	5.0	300	40	—	0.175	36	9	1600	590	3.6	13.3	330	—	2.1	0.49	460	360
			Ca	Mg	Ba*	Co*	Cr	Cs*	Cu*	Fe	Mn*	Ni*	Pb*	Rb*	Sr*	Ti	Th*	U*	V*	Zn*
Shen Ramon																				
		Q.S-1	414	4.0	79	—	—	—	14	8.9	4738	77.1	33.9	23.4	322	—	576	72	—	650
		Q.S-4	1473	14.7	3116	—	—	—	36	8.9	4861	74.0	5.3	25.1	1935	—	61	14	—	259
		Q.S-5	235	8.7	1431	—	—	—	27	5.1	6322	49.4	81.0	6.7	679	—	37	55	—	1046
		Q.S-6	161	9.5	1940	—	—	—	77	34.3	18003	273.6	27.7	7.9	807	—	173	11	—	1617
Kurnub gw																				
		EY6	220	95	42	—	—	—	3.1	bdl	1.52	7.4	0.0071	28	5800	—	0.014	0.003	—	17.7
		Par20	280	90	45	—	—	—	3.4	bdl	0.55	1.13	0.073	31	6500	—	0.017	0.004	—	17.0
		Yaal6a	90	50	60	—	—	—	1.74	0.21	0.37	4.5	0.0096	12.3	1750	—	0.013	0.033	—	7.3
		Grof4	280	105	24	—	—	—	2.3	bdl	0.11	1.75	bdl	19.8	6400	—	0.26	5.3	—	14.1
		Ktur5	230	88	37	—	—	—	3.6	bdl	0.072	0.80	0.031	17.2	4200	—	0.027	2.6	—	13.2
		Shiz1	330	105	32	—	—	—	5.2	1.21	1.66	11.5	0.190	45	8500	—	0.051	0.036	—	28
		Zofar20	950	200	80	—	—	—	21	4.2	644	32	0.106	79	26000	—	0.115	0.008	—	29

(*continued on next page*)

Table 1 (*continued*)

		Ca%	Mg%	Ba	Co	Cr	Cs	Cu	Fe	Mn	Ni	Pb	Rb	Sr	Ti	Th	U	V	Zn
Judea desert																			
Limestone	Bq-2-r	20	0.2	14.9	0.37	—	0.004	0.42	bdl	6.9	2.8	0.112	0.092	—	—	0.054	0.98	11.4	4.1
Limestone	Bq-5-r	50	0.4	14.6	0.76	—	0.499	0.49	98	11.8	7.4	0.120	0.153	230	—	0.069	3.8	15.6	11.4
Dolomite	Da-8-r	30	11	34	0.60	—	0.029	2.5	550	91	18.0	0.166	0.42	—	—	0.23	2.2	22	31
Dolomite	Da-10-r	20	8	30	0.69	—	0.030	3.4	310	105	20	0.177	0.43	—	—	0.193	2.7	22	47
Dolomite	Da-23-r	30	10	39	0.71	—	0.024	5.6	620	34	16.1	0.30	0.36	—	—	0.21	1.64	27	25
Dolomite	Da-27-r	30	11	34	1.14	—	0.027	4.0	950	47	19.2	0.40	0.39	—	—	0.26	2.1	30	34

Texture, texture of the dolomite mineralization, see text for details. Form, stratigraphic formation. If not mentioned otherwise, all concentrations are in ppm, *, ppb; %, weight percent. All samples except Shen Ramon were dissolved completely, Shen Ramon data was obtained after leaching the samples in, pH 1, HNO_3.

Table 2
Sr and Pb isotopic ratios of sampled rocks and water

Location	Texture, form	Sample	$^{208}Pb/^{204}Pb$	s ($\times10^{-3}$)	$^{207}Pb/^{204}Pb$	s ($\times10^{-3}$)	$^{206}Pb/^{204}Pb$	s ($\times10^{-3}$)	$^{87}Sr/^{86}Sr$	s ($\times10^{-5}$)
Dolomite										
ZH	SZFD, Ora	00/05	38.60	2	15.67	0.6	18.54	0.5	0.70790	0.6
ZH	SZFD, Ora	00/06	38.60	10	15.68	2	18.61	4	0.70789	1
ZH	SZFD, Ora	00/07	38.60	6	15.66	2	18.55	2	0.70774	1
ZH	SZFD, Ora	00/08	38.60	10	15.67	4	18.88	4	0.70760	0.6
ZH	SZFD, Ora	00/09	38.70	3	15.72	1	18.56	1	0.70790	1
ZH	SZFD, Ora	00/10	38.60	7	15.67	2	18.57	2		
ZH	SZFD, Ora	00/11	38.60	5	15.68	2	18.50	2		
ZH	SZFD, Ora	00/12	38.70	9	15.67	3	18.58	3		
ZH	SZFD, Ora	00/13	38.70	10	15.69	4	18.69	4		
ZH	SZFD, Ora	00/15	38.80	7	15.69	2	18.71	2		
ZH	NFD, Grofit	00/25	39.00	9	15.80	5	20.94	4	0.70750	0.5
ZH	NFD, Grofit	03/113	38.70	5	15.69	2	18.57	2	0.70803	1
ZH	NFD, Grofit	03/114	38.70	1	15.70	0.4	18.65	0.3		
ZH	NFD, Grofit	03/115	38.50	20	15.67	6	18.92	4	0.70815	7
ZH	NFD, Grofit	03/117	38.80	8	15.75	3	20.47	0.04	0.70814	2
Mt. Eshet	SZFD, Grofit	01/58	38.90	10	15.73	6	19.37	7	0.70792	2
Mt. Eshet	SZFD, Grofit	01/64	38.60	3	15.67	1	18.66	1	0.70799	1
Mt. Eshet	CZFD, Tamar	01/77	38.30	10	15.85	4	22.77	9	0.70855	4
Mt. Eshet	CZFD, Tamar	02/80	38.50	20	16.10	10	27.85	20	0.70838	0.6
Mt. Eshet	CZFD, Tamar	02/81	38.90	20	16.03	7	25.71	10	0.70853	1
Mt. Eshet	CZFD, Tamar	02/82	38.80	8	15.99	3	24.69	5	0.70856	1
Mt. Eshet	CZFD, Ora	02/83	38.70	5	15.84	2	22.24	2	0.70859	1
Mt. Eshet	CZFD, Ora	02/84	38.70	20	15.70	8	19.82	8	0.70855	2
Mt. Eshet	CZFD, Ora	02/86	38.90	3	15.73	1	19.73	1	0.70837	1
Mt. Eshet	CZFD, Ora	02/87	38.80	10	16.09	5	27.41	8	0.70871	1
Mt. Eshet	CZFD, Ora	02/91	38.60	10	15.78	5	21.29	6		
Mt. Eshet	CZFD, Ora	02/92	38.70	4	15.83	2	22.09	2		
Mt. Eshet	CZFD, Ora	02/95	38.60	20	15.83	7	22.27	9	0.70893	2
Mt. Eshet	CZFD, Tamar	02/98	38.90	20	15.71	8	19.70	8		
Mt. Eshet	SZFD, Grofit	02/100	38.80	7	15.69	2	18.70	2		
Mt. Eshet	SZFD, Grofit	02/101	38.90	3	15.70	1	18.86	1		
Mt. Eshet	SZFD, Grofit	02/102	38.80	30	15.68	8	18.81	9	0.70796	2
Mt. Eshet	SZFD, Grofit	02/104	38.90	8	15.69	2	18.82	2		
Mt. Eshet	SZFD, Grofit	02/106	38.90	20	15.67	5	18.88	6		
Mt. Eshet	CZFD, Tamar	03/122	38.80	9	15.80	5	21.46	4		
Mt. Eshet	CZFD, Tamar	03/123	38.70	20	15.98	10	25.57	8		
Mt. Eshet	CZFD, Tamar	03/124	38.60	20	16.12	10	27.80	9	0.70853	1
Mt. Eshet	CZFD, Tamar	03/125	38.80	7	15.90	5	23.61	3		
Mt. Eshet	CZFD, Tamar	03/126	38.70	70	16.27	50	31.58	30		
Eshet Dome	Ora	00/28	38.60	20	16.14	20	28.77	9	0.70830	8
Eshet Dome	CZFD, Tamar	00/34	38.70	10	15.91	9	23.43	6	0.70832	0.6
Eshet Dome	CZFD, Tamar	00/35	38.70	6	15.77	3	20.47	2		
Eshet Dome	CZFD, Tamar	00/38	38.30	40	15.82	30	24.74	20		
Eshet Dome	CZFD, Tamar	00/40	38.70	30	16.22	20	30.46	10	0.70835	1
Eshet Dome	CZFD, Tamar	00/41	38.80	6	15.72	3	19.16	2	0.70796	1
Eshet Dome	CZFD, Tamar	00/43	38.80	9	15.70	3	19.01	3	0.70806	1
Eshet Dome	CZFD, Ora	03/131	38.80	2	15.74	0.6	19.44	1		
Eshet Dome	CZFD, Ora	03/132	38.80	1	15.75	1	20.07	0.6	0.70804	1
Eshet Dome	CZFD, Ora	03/133	38.70	10	15.75	4	20.49	4		
Eshet Dome	CZFD, Ora	03/134	38.80	9	15.87	5	22.42	4	0.70810	0.5
Eshet Dome	CZFD, Ora	03/135	38.80	8	15.73	2	19.54	3	0.70802	1
Eshet Dome	CZFD, Ora	03/136	38.80	8	15.80	3	20.86	3	0.70796	1
Eshet Dome	CZFD, Tamar	03/146	38.90	10	15.78	5	20.84	4		
Eshet Dome	CZFD, Tamar	03/147	38.90	10	15.69	5	18.93	4		
Eshet Dome	CZFD, Tamar	03/148	38.90	5	15.72	2	19.27	1		
Eshet Dome	CZFD, Tamar	03/149	38.80	2	15.71	1	19.11	1		
Eshet Dome	CZFD, Tamar	03/156	38.70	1	15.72	0.6	19.33	0.5		
Eshet Dome	CZFD, Tamar	03/158	38.70	8	15.72	2	19.50	2		
Eshet Dome	CZFD, Tamar	03/159	38.60	10	15.75	4	20.26	4		
Eshet Dome	CZFD, Tamar	03/160	38.70	2	15.72	1	19.37	1		
Eshet Dome	CZFD, Tamar	03/161	38.70	10	15.78	7	20.69	5		

(*continued on next page*)

Table 2 (*continued*)

Location	Texture, form	Sample	$^{208}Pb/^{204}Pb$	s ($\times10^{-3}$)	$^{207}Pb/^{204}Pb$	s ($\times10^{-3}$)	$^{206}Pb/^{204}Pb$	s ($\times10^{-3}$)	$^{87}Sr/^{86}Sr$	s($\times10^{-5}$)
Fe-oxides										
ZH	Ora	00/01	38.60	3	15.66	1	18.47	1	0.70787	4
ZH	Ora	00/02	38.60	4	15.68	2	18.45	2	0.70818	3
ZH	Ora	00/04	38.50	1	15.67	0.5	18.44	0.6	0.70826	2
ZH	Ora	00/16	38.50	4	15.65	1	18.45	2	0.70797	5
ZH	Ora	00/17	38.60	20	15.69	7	18.44	6		
ZH	Ora	00/18	38.60	6	15.67	2	18.45	4		
ZH	Ora	00/19	38.60	2	15.67	0.7	18.44	1	0.70783	4
ZH	Ora	00/20	38.50	6	15.65	2	18.41	2		
ZH	Ora	00/22	38.60	5	15.69	2	18.49	3	0.70818	5
ZH	Ora	00/47	38.60	2	15.67	0.9	18.44	1	0.70810	2
ZH	Ora	01/69	38.50	1	15.67	0.4	18.44	0.5	0.70791	10
ZH	Ora	01/70	38.50	4	15.67	2	18.42	2		
ZH	Ora	01/71	38.50	20	15.64	6	18.43	5		
ZH	Ora	01/75	38.60	3	15.67	1	18.45	1	0.70826	2
ZH	Ora	01/76	38.50	2	15.66	0.7	18.45	0.7		
ZH	Ora	03/118	38.80	3	15.73	8	18.57	7	0.70803	3
ZH	Ora	03/119	38.70	40	15.71	10	18.52	10	0.70791	8
ZH	Ora	03/120	38.60	4	15.68	1	18.52	1		
ZH	Ora	03/121	38.70	30	15.72	10	15.72	8	0.70772	20
Mt. Eshet	Tamar	00/49	38.80	10	15.81	4	21.29	6		
Mt. Eshet	Tamar	01/50	38.50	60	15.69	30	18.74	30	0.70812	7
Mt. Eshet	Tamar	01/51	38.80	20	15.72	9	20.14	10		
Mt. Eshet	Tamar	01/52	38.70	30	15.89	10	22.71	20	0.70814	1
Mt. Eshet	Tamar	01/54	38.70	10	15.71	6	20.26	7		
Mt. Eshet	Tamar	01/55	38.80	30	15.73	10	20.17	20	0.70841	4
Mt. Eshet	Tamar	01/56	39.00	3	15.90	1	22.68	1		
Mt. Eshet	Tamar	01/57	38.80	20	15.85	7	22.45	10	0.70828	2
Mt. Eshet	Grofit	01/61	38.80	10	15.75	4	19.23	4		
Mt. Eshet	Grofit	01/65	38.60	1	15.67	0.5	18.48	0.5	0.70824	4
Mt. Eshet	Grofit	01/66	39.90	200	16.07	50	18.74	40	0.70848	2
Mt. Eshet	Grofit	01/67	38.70	2	15.68	0.6	18.58	1	0.70818	1
Mt. Eshet	Grofit	02/103	38.90	3	15.70	1	18.85	0.5	0.70795	2
Mt. Eshet	Grofit	02/105	38.90	6	15.69	2	18.84	1		
Eshet Dome	Tamar	00/32	38.80	20	15.99	10	25.12	10	0.70815	1
Eshet Dome	Tamar	00/33	38.90	20	15.76	8	20.49	8		
Eshet Dome	Tamar	00/36	38.80	10	15.70	4	19.45	4	0.70832	1
Eshet Dome	Tamar	00/37	38.80	10	15.77	5	20.56	5	0.70857	2
Eshet Dome	Tamar	00/39	38.90	40	15.73	20	19.30	20	0.70831	5
Eshet Dome	Tamar	03/162	39.10	7	16.04	2	25.04	3		
Eshet Dome	Tamar	03/163	38.90	8	15.91	4	22.66	10	0.70832	1
Eshet Dome	Tamar	03/164	38.80	20	15.97	9	25.07	10		
Eshet Dome	Tamar	03/165	38.70	20	15.85	7	22.83	10	0.70850	2
Eshet Dome	Tamar	03/166	38.90	7	15.80	3	21.40	4	0.70830	1
Eshet Dome	Tamar	03/167	38.80	5	15.92	2	24.07	2		
Eshet Dome	Tamar	03/168	39.00	3	15.74	1	19.30	1		
Eshet Dome	Tamar	03/169	39.00	2	15.82	1	21.19	1		
Eshet Dome	Tamar	03/170	38.80	3	15.68	1	19.09	2		
Host rock limestone and digenetic dolomite										
ZH	Grofit	00/24	38.90	10	15.78	6	20.70	5	0.70745	0.5
Eshet Dome	Tamar	00/26	38.70	20	15.95	10	24.71	20	0.70759	1
Eshet Dome	Tamar	00/30	38.80	10	16.05	8	26.44	10	0.70751	1
Mt. Eshet	Grofit	03/128	38.40	20	16.18	7	30.22	10	0.70751	2
Govai Mnt.	Ora	03/130	38.80	3	15.68	1	19.02	1	0.70745	1
Ashosh plug										
		Ash171	38.89	2	15.63	1	18.32	1	0.70504	1
		Ash172	38.76	2	15.59	1	18.26	1	0.70527	3
		Ash173	38.78	2	15.61	0.5	18.32	1	0.70500	1
		Ash174	38.80	2	15.60	1	18.28	1	0.70511	1
		Ash175	38.81	1	15.61	0.5	18.28	0.6	0.70508	1

Table 2 (*continued*)

Location	Texture, form	Sample	$^{208}Pb/^{204}Pb$	s ($\times10^{-3}$)	$^{207}Pb/^{204}Pb$	s ($\times10^{-3}$)	$^{206}Pb/^{204}Pb$	s ($\times10^{-3}$)	$^{87}Sr/^{86}Sr$	s ($\times10^{-5}$)
Shen Ramon										
		Q.S-1	38.69	0.2	15.63	1	18.32	1	0.70868	5
		Q.S-4	38.73	1	15.64	5	18.84	6	0.70833	1
		Q.S-5	38.31	0.5	15.66	2	18.71	2	0.70881	2
		Q.S-6	39.78	2	15.66	8	19.74	10	0.70832	1
Kurnub Aq.										
		EY6							0.70767	
		Par20							0.70739	
		Yaal6a							0.70778	
		Grof4							0.70734	
		Ktur5							0.70734	
		Shiz1	37.70	1	15.50	4	17.86	5	0.70733	
		Zofar20	37.70	2	15.55	6	17.86	8	0.70791	
Judea desert										
	Limestone	Bq-1-r	37.51		15.68		26.75		0.70755	4
	Limestone	Bq-2-r	38.71		15.93		25.67		0.70742	1
	Limestone	Bq-3-r	38.32		16.06		27.27		0.70775	5
	Dolomite	Da-8-r	38.80		16.04		26.75		0.70793	1
	Dolomite	Da-10-r	38.81		16.10		27.99		0.70800	0.6
	Dolomite	Da-23-r	38.19		15.76		22.07		0.70790	0.6
	Dolomite	Da-3-r	38.76		16.37		32.10			
	Dolomite	Da-6-r	38.92		16.73		41.55			
	Dolomite	Da-7-r	38.86		16.79		42.83			
	Dolomite	Da-9-r	39.07		16.20		29.78			
	Dolomite	Da-16-r	38.91		16.18		28.79			
	Dolomite	Da-25-r	38.99		16.10		27.77			
	Dolomite	Da-27-r	38.86		16.02		26.97			
	Limestone	Bq-5-r	39.06		16.82		42.19			
	Limestone	Bq-8-r	39.38		16.31		29.73			
	Limestone	Bq-10-r	39.00		16.22		31.37			

Shen Ramon data were obtained after leaching the samples in, pH 1, HNO_3.

The isotopic composition of Pb, i.e., $^{208}Pb/^{204}Pb$, $^{207}Pb/^{204}Pb$, and $^{206}Pb/^{204}Pb$ ratios, were measured in the same dolomite and Fe-oxide samples analyzed for strontium isotopes. Similar to the $^{87}Sr/^{86}Sr$ values, ZH, the westernmost site which is furthest from the Dead Sea Rift, has the least radiogenic values (Figs. 1, 3, and 4). The $^{207}Pb/^{204}Pb$ and $^{206}Pb/^{204}Pb$ ratios from all three sites

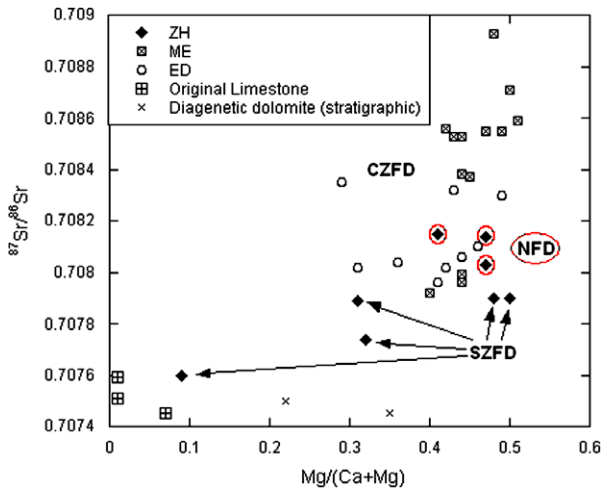

Fig. 3. $^{87}Sr/^{86}Sr$ vs. Mg/(Ca+Mg) in carbonates from the study area. The epigenetic dolomites show a correlation of increasing $^{87}Sr/^{86}Sr$ with increasing Mg-content while the diagenetic dolomite (early dolomitization) show high Mg-content but low $^{87}Sr/^{86}Sr$, similar to the original rock Sr composition. SZFD, simple-zoned ferroan dolomite; CZFD, complex-zoned ferroan dolomite; NFD, non-ferroan dolomite.

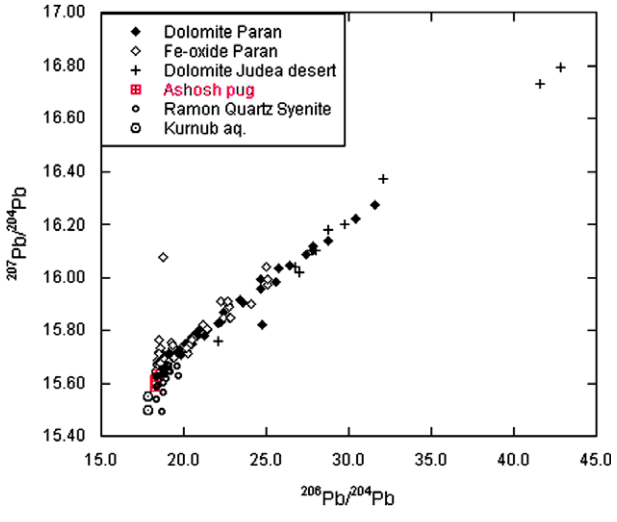

Fig. 4. $^{207}Pb/^{204}Pb$ vs. $^{206}Pb/^{204}Pb$ in dolomites and Fe-oxides from the study area and Pb isotopic compositions of suggested sources to the mineralization (end-members). The straight line obtained from the dolomite and Fe-oxide samples is a result of mixing. Dolomite Judea desert = discordant epigenetic dolomites of the Judea Group carbonates along the Dead Sea.

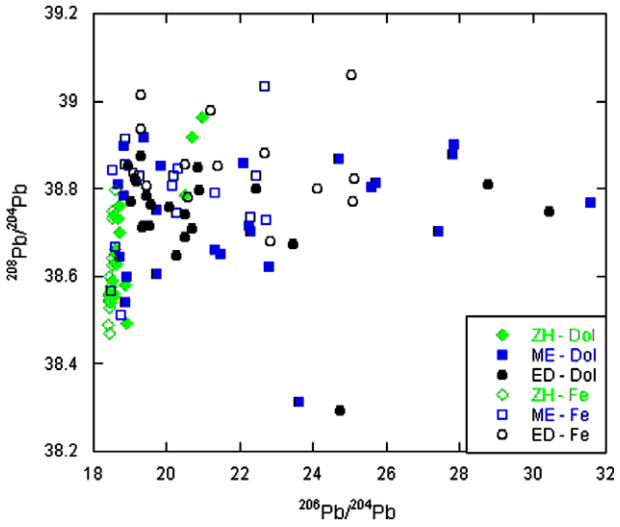

Fig. 5. $^{208}Pb/^{204}Pb$ vs. $^{206}Pb/^{204}Pb$ in dolomites and Fe-oxides from the study area.

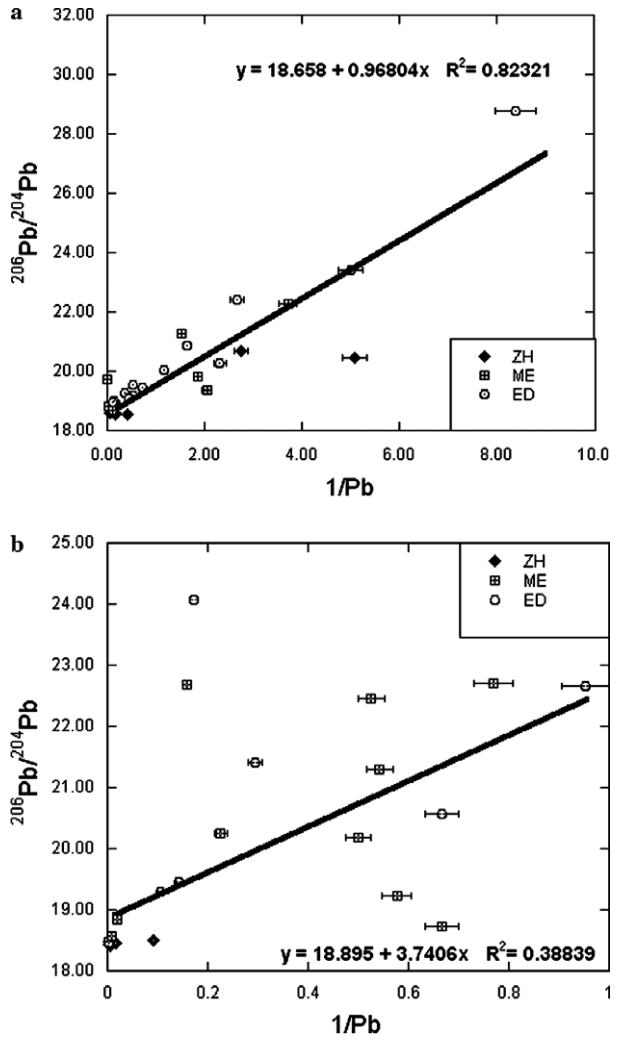

Fig. 6. Pb isotopic composition vs. 1/[Pb]. (a) $^{206}Pb/^{204}Pb$ vs. 1/[Pb] in dolomites, (b) $^{206}Pb/^{204}Pb$ vs. 1/[Pb] in Fe-oxides.

along the Paran fault in both the Fe-oxides and dolomite samples plot on a straight line (Fig. 4). On the other hand, $^{208}Pb/^{204}Pb$ values do not correlate with either $^{207}Pb/^{204}Pb$ or $^{206}Pb/^{204}Pb$ values (Fig. 5). Thus, in contrast to Sr isotopes, $^{206}Pb/^{204}Pb$ and $^{207}Pb/^{204}Pb$ vs. 1/Pb relations in dolomites and to a lesser degree in Fe-oxides suggest that mixing between two end-members controls the behavior of Pb in the mineralization products along the Paran fault (Fig. 6; Table 2).

5. Discussion

The present study aims to identify the types of groundwater that caused the mineralization phenomenon along the Paran fault and to determine the sources of the metallic enrichments in the epigenetic minerals. We first address the epigenetic dolomites (non-ferroan, complex-zoned ferroan, and simple-zoned ferroan dolomites), then consider the Fe-oxides associated with the ferroan dolomites, and the timing and types of association. This characterization allows us to describe the regional flow paths and sub-surface conditions which caused the mineralization along the Paran fault.

5.1. Epigenetic dolomitization and Fe-oxides within the ferroan dolomites

The $^{87}Sr/^{86}Sr$ values in the dolomite samples (0.7076–0.7089) are significantly higher than the values of marine Cenomanian–Turonian carbonates (0.7074–0.7076; Hess et al., 1986) (Fig. 7). The $^{87}Sr/^{86}Sr$ values of the Paran mineralized samples are similar to those found in discordant epigenetic dolomite rock bodies in the same rock sequence (Judea Group of Cenomanian–Turonian age) along the Dead Sea Rift (Table 2; Fig. 7; Stein et al., 2002). Evaporite and dolomite layers from the Pleistocene Sedom Formation also have $^{87}Sr/^{86}Sr$ values which range from 0.7082 to 0.7086 (Stein et al., 2000; Fig. 7). In addition, contemporary spring waters along the Dead Sea shores have $^{87}Sr/^{86}Sr$ values of 0.7079–0.7080 (Stein et al., 1997). Indeed, interaction between the Judea Group carbonates with the Late Miocene–Pliocene Sedom Lagoon evaporated seawater in the sub-surface was proposed to have determined the $^{87}Sr/^{86}Sr$ values of these epigenetic dolomite bodies (Starinsky, 1974; Stein et al., 2000, 2002).

Values of $^{206}Pb/^{204}Pb$ vs. $^{207}Pb/^{204}Pb$ of the mineralized Paran carbonates plot along the same linear trend as the discordant epigenetic dolomite rock samples from the Dead Sea Rift (Judean dolomites, Fig. 4). Although the Dead Sea samples are on average more radiogenic, there is a substantial overlap in their values (Fig. 4). Moreover, $^{206}Pb/^{204}Pb$ and $^{207}Pb/^{204}Pb$ values indicate a two end-member mixing where the Dead Sea samples plot on the radiogenic end (Figs. 4–6). Thus, it is possible that the same type of waters, i.e., Dead Sea brines, were responsible for the radiogenic Sr and Pb values and Mg enrichment in the discordant epigenetic dolomites of the Judea Group

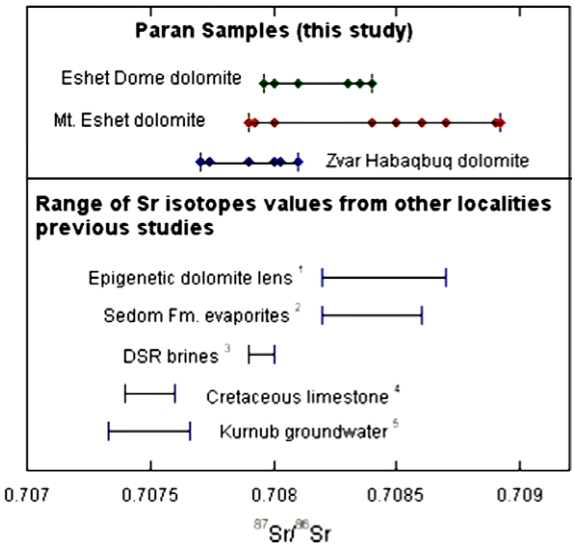

Fig. 7. Diagram illustrating the general ranges of strontium isotope ratios at the three sample sites and potential source rocks and fluids.

carbonates along the Dead Sea and along the Paran Fault in the Menuha Ridge area.

It is important to stress the difference between the sources of radiogenic Sr and Pb in the Dead Sea brines. Whereas, Sr obtained its radiogenic values from the evaporated Pliocene marine waters ($^{87}Sr/^{86}Sr = 0.7090$; DePaolo, 1986), radiogenic $^{206}Pb/^{204}Pb$ and $^{207}Pb/^{204}Pb$ values originate from the Cenomanian–Turonian marine carbonates that were leached by the Dead Sea brines. Marine waters and hence marine carbonates have high U and low Pb and Th concentrations (Whitfield and Turner, 1987). Therefore the ~100 Myr high U, low Pb and low Th carbonates have radiogenic $^{206}Pb/^{204}Pb$ and $^{207}Pb/^{204}Pb$ values, but low $^{208}Pb/^{204}Pb$ values (Moorbath et al., 1987; Jahn and Simonson, 1995). The Dead Sea brines probably preferentially leached radiogenic $^{206}Pb/^{204}Pb$ and $^{207}Pb/^{204}Pb$ from the α-recoil damaged carbonates (Harlavan et al., 1998), thus, increasing $^{206}Pb/^{204}Pb$ and $^{207}Pb/^{204}Pb$ values in the dolomites relative to the limestone country rock (Table 2). Furthermore, even in the dolomite-free country rock near the Paran fault there is an indication for a resetting of Pb isotopic ratios, as the more radiogenic values of the country rock were detected in the sites with more radiogenic dolomites (ED, EM), and the slope of the ^{207}Pb–^{206}Pb isochrone of the limestone country rock yields a negative age (Table 2).

The $^{87}Sr/^{86}Sr$ values of the Fe-oxides (0.7077–0.7086) are similar to the values of their ferroan dolomite hosts. Based on the protocol described in the methods section, secondary calcite was removed from the Fe-oxides prior to their dissolution. Since the Sr/Ca ratio in the Fe-oxides is higher than in secondary calcite (Table 1), it can be assumed that the isotopic composition of Sr released during Fe-oxide dissolution indeed represents Sr embedded in the Fe oxides and not Sr released from the secondary calcite. As for the dolomites, $^{87}Sr/^{86}Sr$ and Sr concentrations in Fe-oxides do not indicate a simple mixing between two end-members. On the other hand, $^{206}Pb/^{204}Pb$ and $^{207}Pb/^{204}Pb$ in the Fe-oxides show a moderate linear trend when plotting the isotopic values against 1/[Pb] ($R^2 = 0.39$ and 0.45, respectively; Fig. 6; Tables 1 and 2). The fact that the mixing line of Pb in the Fe-oxides is less well defined than in the dolomites is the result of the low-range of Pb concentrations and isotopic values in Fe-oxides (Tables 1 and 2).

5.2. Sr and Pb isotopes, rock petrography, and source apportionment

One of the most interesting observations of the current study is the correspondence between the isotopic composition of Sr and Pb and the petrography of the mineralized rock. The $^{206}Pb/^{204}Pb$ and $^{207}Pb/^{204}Pb$ values in the Fe-oxides (and dolomites) of the simple-zoned ferroan dolomites, plot at the Pb-rich, non-radiogenic end-member side of the mixing line (Fig. 8). Moreover, Pb in the simple-zoned ferroan Fe-oxides plot along the "Geochron" while all other samples have anomalous Pb (Faure, 1986). The $^{206}Pb/^{204}Pb$ and $^{207}Pb/^{204}Pb$ values of the simple-zoned ferroan samples with the least radiogenic Pb are similar to values in two igneous bodies exposed at the vicinity of the Paran fault (Fig. 4; Table 2). Ashosh plug is a 20.7 ± 2.2 Myr labradorite–andesine basalt with xenoliths of gabbro, exposed in the Arava valley 20 km north of the Paran fault (Levite, 1966; Steinitz and Bartov, 1991). Its $^{206}Pb/^{204}Pb$ values range between 18.26 and 18.42 and $^{207}Pb/^{204}Pb$ values between 15.59 and 15.63 (Table 2). As expected for basaltic rock, the $^{87}Sr/^{86}Sr$ values of the Ashosh plug are also non-radiogenic and range between 0.70500 and 0.70742 (Table 2). The other igneous rock measured in this study was the nearby Ramon intrusion (~ 40 km north of the Paran Fault), a 124 ± 13 Myr quartz syenite (Bentor, 1952; Lang

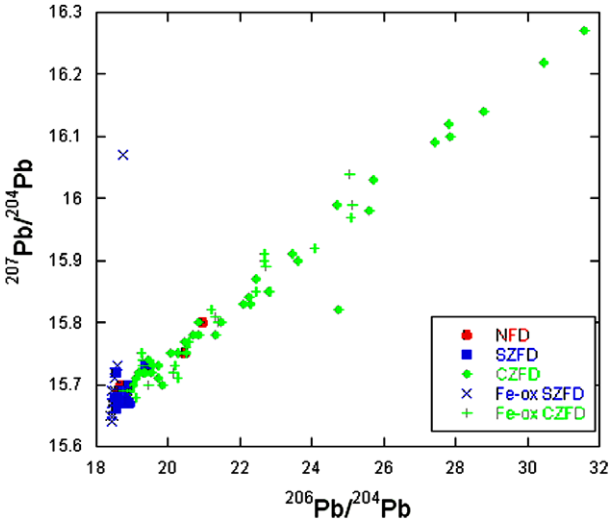

Fig. 8. $^{207}Pb/^{204}Pb$ vs. $^{206}Pb/^{204}Pb$ of rocks according to their petrographic characterization. SZFD, simple-zoned ferroan dolomite; CZFD, complex-zoned ferroan dolomite; NFD, non-ferroan dolomite.

et al., 1988), partially altered by hydrothermal fluids. The $^{206}Pb/^{204}Pb$ values of the Ramon intrusion varies between 18.32 and 19.74, and the $^{207}Pb/^{204}Pb$ between 15.63 and 15.66 (Table 2). These syenitic igneous rocks have significantly higher $^{87}Sr/^{86}Sr$ ratios than Ashosh plug, ranging between 0.70832 and 0.70881 (Table 2). Although the Ramon intrusion is exposed in a different tectonic province than the Paran fault, other intrusions with similar composition to the Ramon were identified in the sub-surface in the region between the Ramon intrusion and the Paran fault (Gvirtzman et al., 1994). Similar Pb and Sr isotopic values also appear in present-day groundwater from the Lower Cretaceous Kurnub Group aquifer (Table 2; Henig, 2004). All the igneous rock and the groundwater values plot at the non-radiogenic end-member of $^{206}Pb/^{204}Pb$ vs. $^{207}Pb/^{204}Pb$ line occupied by Pb in simple-zoned Fe-oxides (Fig. 4), suggesting that they contributed Pb (and possibly other metals enriched in the ferroan dolomites such as Fe, Cu, Mn, Ni, V, Zn, and U) to the mineralization process along the Paran fault. Examination of the Pb isotope values in Table 2 also reveals why $^{208}Pb/^{204}Pb$ ratios do not indicate any mixing (Fig. 5). Both radiogenic and non-radiogenic end-members have very similar $^{208}Pb/^{204}Pb$ ratios, and hence the entire range of $^{208}Pb/^{204}Pb$ values is very narrow and the corresponding uncertainty in the isotopic values is rather large (Fig. 5).

Whereas $^{206}Pb/^{204}Pb$ and $^{207}Pb/^{204}Pb$ indicate mixing between two distinct end-members, there is no linear relationship between $^{87}Sr/^{86}Sr$ ratios and 1/[Sr] (Table 2). Both Sr and Pb in the mineralization products along the Paran Fault are contributed by at least four end-members: at least two types of igneous rocks, including the weathering products of the igneous basement in the Nubian rocks. Based on the rocks outcropped in the nearby Timna region, the igneous basement in the Paran region is composed of basic and ultra-basic pyroxene hornblende-olivine norite, intermediate rocks such as diorite, calc-alkaline granite, perthitic alkaline granite, and dolorite dikes, effected by alteration processes (Beyth and Reischman, 1996; Segev et al., 1999). Other members are evaporated marine waters (Dead Sea brines), and the original Cenomanian–Turonian carbonates. Since both types of igneous rocks have similar isotopic values of Pb and (they are both non-radiogenic) and have similar high Pb concentrations, they converge into one end-member. Dead Sea brines have very low concentrations of Pb and acquire their Pb-content and radiogenic $^{206}Pb/^{204}Pb$ and $^{207}Pb/^{204}Pb$ values from the leached Cenomanian–Turonian carbonates. As a result, the four Pb end-members in practice congregate into two end-members with different Pb-content and different $^{206}Pb/^{204}Pb$ and $^{207}Pb/^{204}Pb$ values. On the other hand, the $^{87}Sr/^{86}Sr$ values of the two types of igneous rocks are very different, and both evaporated marine waters and Cenomanian–Turonian carbonates have high Sr concentrations but different $^{87}Sr/^{86}Sr$ values. Therefore, Sr in the dolomitized rocks of the Paran fault is affected by all four end-members and does not display the type of relationship expected from a mixture of two end-members. The mixing of Dead Sea brines with another type of water in the sub-surface is observed also in present-day Nubian aquifer waters. At least one drill hole (Zofar 20, located 22 km north of Menuha Ridge) from the Nubian aquifer contains an appreciable amount of Ca-chloride saline water typical of the Dead Sea brines (Starinsky, 1974). The measured $^{87}Sr/^{86}Sr$ value of water sampled in this location (0.70791; Table 2) is significantly higher than the $^{87}Sr/^{86}Sr$ values typical of Nubian aquifer waters (0.7073–0.7077; Henig, 2004).

In summary, the Pb and Sr isotope data indicate that two groundwater types were involved in the dolomitization and mineralization along the Paran fault. The first one was a Mg-rich brine that originated from the Late Miocene–Pliocene Sedom lagoon with radiogenic Sr that migrated through the carbonate section along the Dead Sea Rift to the Paran area preferentially leaching radiogenic Pb from the carbonate bedrock. The second groundwater obtained its dissolved constituents from leaching of the underlying igneous basement rocks and clastic sandstones.

5.3. Timing and types of mineralization and regional flow paths

Previous research, including geochemical and modeling studies have suggested long range sub-surface migration of Dead Sea brines (Starinsky, 1974; Stanislavsky and Gvirtzman, 1999). Given that mineralized clasts are found in the Mid-Late Pliocene sediments (Arava Formation; Avni, 1997; Avni et al., 2001), this would place the mineralization as being contemporaneous with the Late Miocene–Early Pliocene formation of the Sedom Lagoon (6–3 Ma). This timing is critical for the mineralization because at this time the Dead Sea—Arava depression had not yet reached the Paran area and the topographic hydrologic head was to the east in the Edom Mountains (Avni et al., 2000; Ginat et al., 2000). This would have allowed westward sub-surface flow of meteoric ground water, rather than from (or in addition) the south as proposed in previous studies, which would have acquired its composition from leaching of igneous rocks and clastic sediments. This type of groundwater was initially present in the sub-surface as formation waters (Ilani et al., 1988), and became enriched in Fe, Pb, and other cations. Indeed, modeling studies of Stanislavsky and Gvirtzman (1999) indicate that the first pulses of density driven migration of Dead Sea Brines would have expelled formation waters ahead of them. The association between these types of sub-surface fluids and their interactions as reflected in the secondary minerals along the Paran fault will be discussed next.

Oxygen isotope analyses of dolomites fall into two groups: (1) 'high $\delta^{18}O$' dolomites characterized by $\delta^{18}O$ SMOW values varying from 27 to 30.5‰ and (2) 'low $\delta^{18}O$' dolomites, characterized by $\delta^{18}O$ variation from 18 to 25‰. High $\delta^{18}O$ dolomites primarily comprise simple-

zoned dolomites and non-ferroan dolomites sampled at ZH and the *Gerofit* Formation rocks at ME (Grosz et al., 2006). The isotopically light dolomites comprise the complex-zoned dolomites (Cenomanian *Tamar* Formation rocks at ME and ED and Vroman Bank at ME). Thus, the low $\delta^{18}O$ values are associated with the dolomites showing the most extensive history of epigenetic dolomitization (see Introduction). Grosz et al. (2006) interpreted these isotopic variations primarily to reflect an increase of temperature during dolomitization (from <50 to 75 °C) together with lowering in the $\delta^{18}O$ SMOW value of the fluid during dolomitization, from an initial value of *ca* 0‰ to values of—4‰ or lower; the lower values reflecting a larger component of recharge meteoric water compared to continental formation waters and brines (cf. Fleischer et al., 1977).

As indicated earlier, the petrographic classification of dolomites is also reflected in their Pb and Sr isotope ratios: complex-zoned ferroan dolomites have higher $^{206}Pb/^{204}Pb$, $^{207}Pb/^{204}Pb$, and $^{87}Sr/^{86}Sr$ ratios than simple-zoned and non-ferroan dolomites (Figs. 3 and 8). Fig. 9 plots the Pb isotope ratio ($^{206}Pb/^{204}Pb$) of dolomites against their $\delta^{18}O$ SMOW values. Generally, the data show that $\delta^{18}O$ decreases as the $^{206}Pb/^{204}Pb$ ratio increases. The ZH and ME samples define a smooth trend characterised by an initial decrease of $\delta^{18}O$ at low (non-radiogenic) Pb isotope ratios followed by a marked increase of the radiogenic Pb for the lowest $\delta^{18}O$ dolomites. This suggests that the isotopic trends can be modelled by mixing between radiogenic and non-radiogenic Pb isotope end-members and high and low $\delta^{18}O$ dolomite end-members. Curves illustrating possible mixing relations are made here for end-member fluids with $^{206}Pb/^{204}Pb$ ratios of 18.0 and of 43.0, respectively, and corresponding dolomite $\delta^{18}O$ values = 31‰ and 18‰, respectively. The non-radiogenic and radiogenic Pb isotopic end-members correspond to the igneous/clastic sediment and Dead Sea Rift components in Table 2. The high and low $\delta^{18}O$ end-members correspond to dolomites in oxygen isotope equilibrium with groundwater with $\delta^{18}O = 0‰$ and −4‰ at temperatures of 25 and 75 °C, respectively. The mixing lines are plotted for solution concentration ratios of the radiogenic/non-radiogenic Pb end-members of 1:20, 1:10, 1:5, 1:2, and 1:1. It can be seen that most of the data are bracketed by the 1:20 and 1:5 radiogenic/non-radiogenic mixing lines. A few of the samples plot close to mixing lines with lower ratios. Indeed the Pb-content of the non-radiogenic end-member (the igneous rocks) is 10–80 times higher than Pb-content of the radiogenic Pb (dolomites from the Judea desert) (Tables 1 and 2).

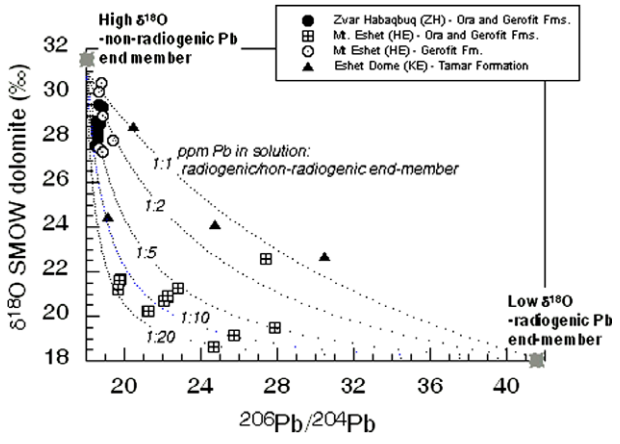

Fig. 9. $^{206}Pb/^{204}Pb$ vs. $\delta^{18}O$ SMOW plot for dolomite samples. Data sources: this work and Grosz et al. (2006). The details of the mixing lines are presented in the text.

The data trends thus suggest that the complex-zoned dolomites occurring at ME and ED reflect the infiltration of large quantities of a radiogenic Pb isotope and higher temperature fluid. In contrast, simple-zoned dolomites reflect a low-temperature-high $\delta^{18}O$ and non-radiogenic Pb-rich fluid. The fact that lower $\delta^{18}O$ values are associated with the radiogenic Pb end-member (of DSR brines) suggests that they were entrained within higher temperature deep-seated groundwater during their transport to the site of mineralization. A gradual deepening of the system (i.e., penetration of the dense Dead Sea brines to deeper aquifers) is consistent with the model calculations of Stanislavsky and Gvirtzman (1999). Therefore, it is possible that the Mg during this initial dolomitization reaction was provided by Mg-rich formation waters leaching the magmatic, Mg-rich bedrock. However, during later stages of mineralization and post dating the formation of the Fe-oxide lenses the Dead Sea fluid end-member became the dominant component of the dolomitization system, causing non-ferroan and complex-zoned ferroan dolomitization. Indeed, the complex-zoned dolomites have the most radiogenic Sr and Pb isotope ratios and the non-ferroan dolomites have intermediate values of both Sr and Pb isotopic ratios (Figs. 3 and 8). This clear distinction between the three types of dolomitization types based on both Sr and Pb isotopes strongly supports the scenario about the order of events and the types of groundwaters involved in the dolomitization and mineralization phenomena along the Paran fault described previously.

These arguments are illustrated by the schematic model summarizing the major fluid flow patterns to the Paran Fault site presented in Fig. 10. Generally westward moving groundwater originating in topographic high recharge areas in the Edom Mountains (and possibly northward moving groundwater from Sinai) moved towards the Paran Fault and mixed with Dead Sea brines that had penetrated south by density driven migration. In the initial phase, non-ferroan dolomites and simple-zoned ferroan dolomites formed from metalliferous groundwaters and formation waters at relatively shallow depths and lower temperatures. With time the

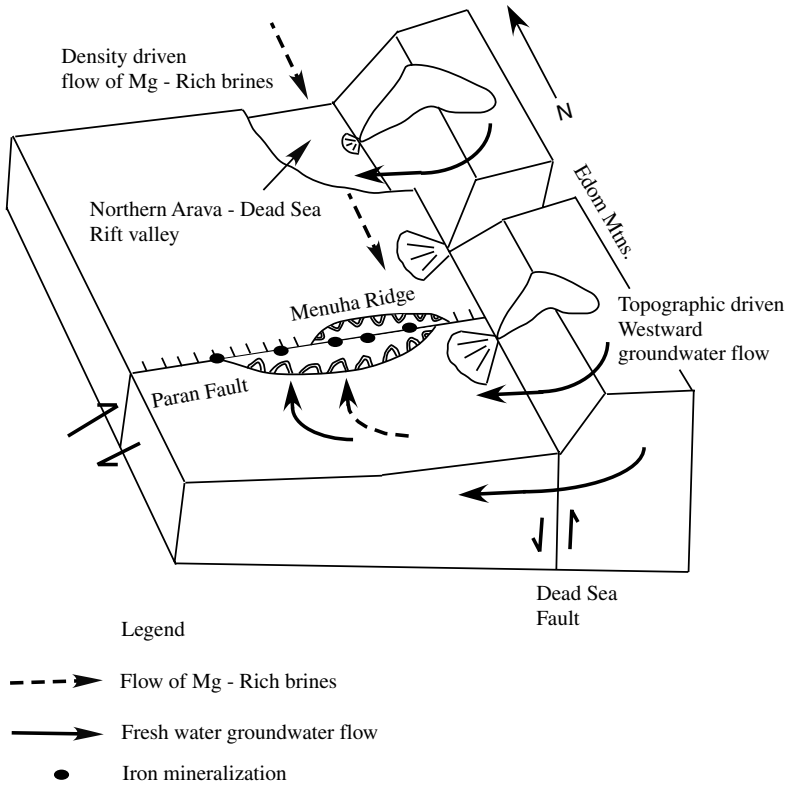

Fig. 10. Schematic model for the flow patterns associated with the development of the Paran Fault mineralization. The cartoon shows the configuration in the Early Pliocene, when the Dead Sea rift depression in which the Sedom lagoons formed was further to the north, but the Paran area was still uplifted and adjacent to the Edom Mountains of Jordan. At this time the Paran area was characterized by westward flowing rivers, with the Menuha Ridge area forming a gently westward-dipping slope (Avni et al., 2000; Ginat et al., 2000). Two major flow paths are envisaged: (i) generally southward density driven migration of the Dead Sea (Sedom) brines; (ii) westward-directed groundwater flow from recharge areas in the Edom Mountains.

Dead Sea brine component increased and the flow patterns became deeper and hotter.

6. Summary and conclusions

This paper combined Pb and Sr isotope measurements with detailed sampling and petrography in order to distinguish between sub-surface fluids involved in large scale dolomite and iron mineralization shear zone faults adjacent to the tectonically active Dead Sea Transform, and to identify the sources of elements enriched in the mineralization. The study identified two potential sources of Pb—a less radiogenic source with Pb isotope composition similar to nearby igneous intrusions, and a more radiogenic source derived from Upper Cretaceous (Cenomanian–Turonian) marine carbonates. Four potential sources of Sr were identified—basaltic igneous intrusions, felsic igneous intrusions, evaporated seawater (Dead Sea brines), and Cenomanian–Turonian carbonates.

According to the geochemical results it is argued that an early, shallow, cool fluid arrived at the Paran Fault after having interacted with igneous rocks to acquire less radiogenic Pb. The strontium in this fluid was a mixture between a less radiogenic component derived from the mafic igneous rocks and a more radiogenic component derived from the felsic rocks. This fluid appears to have been responsible for precipitating the so-called ''simple-zoned ferroan dolomite'' in the mineralization assemblage. The fluid is thought to have been driven westward toward the Paran fault by the topographically high Edom Mountains that border the Dead Sea Rift Valley and from the Sinai Peninsula in the south. This groundwater flowed at shallow depth and the exact timing of the movement of this fluid is not yet clear. A second fluid then began to dominate the mineralizing system and carried more radiogenic Pb and strontium that was a mixture of an evaporated seawater component and a Cenomanian–Turonian carbonate component. This fluid appears to have precipitated the ''complex-zoned ferroan dolomite''. A third dolomite phase, the ''non-ferroan dolomite'', appears to be intermediate to the simple and complex-zoned ferroan dolomites, based on Pb and Sr isotope composition, and thus perhaps a mixing product of the two fluids. The second fluid appears to have originated in the Dead Sea depression as evaporated seawater and descended into the sub-surface due to its high density. Based on the known geological his-

tory of the region and on field observations showing the presence of epigenetic dolomitized clasts in the Late Pliocene Arava conglomerates (but not in Miocene conglomerates), it is suggested that the Dead Sea brines migrated in the Late Miocene–Early Pliocene interval. These brines migrated along a relatively deep path to the site of mineralization and were heated to higher temperatures.

The sub-surface flow systems described in the current paper and the interaction between groundwater related to tectonic activity with the preceding regional groundwater flow is not unique to the Dead Sea Rift. On the contrary, the sub-surface flow system described here is an example for migration patterns of brines originating in tectonic active regions. It has been argued by Bethke and Marshak (1990) that groundwater migration is an important, albeit generally neglected, aspect of plate tectonics. Extensive mineralization phenomena, similar to the ones described in the current paper have been recorded in numerous locations of active tectonics around the World. The topographic head and hydrological gradient critical to fluid migration in the formation of MVT deposits is activated by compressional orogeny that results in thrust faulting and uplift (Garven et al., 1993). The presence of a strongly evaporitic Sabkha environment in the flow path also appears to be necessary for the high salinities required for metal solubility and transport (Sverjensky, 1986; Leach et al., 2001; Robb, 2005). This study shows that tectonic activity related to continental transform faulting and rifting stimulates regional-scale sedimentary mineralization by providing a major evaporative brine source and generating a remarkable interaction between topographically and density-driven groundwater flow systems.

Acknowledgments

The authors thank L. Halitz, S. Ehrlich, O. Yoffe, I. Segal, and N. Tepliakov of the Geological Survey of Israel, R. Nissan of the HU for technical help, and M. Appold and an anonymous reviewer for thoughtful and useful comments. This work was supported by Israel Science Foundation Grant 455/00.

Associate editor: Dimitri A. Sverjensky

References

Appold, M.S., Garven, G., 1999. The hydrology of ore formation in the Southeastern Missouri District; numerical models of topography-driven fluid flow during the Ouchita Orogeny. *Econ. Geol.* **94** (6), 913–935.

Avigour, A., Magaritz, M., Issar, A., 1992. Pleistocene paleoclimate of the arid region of Israel as recorded in calcite deposits along regional transverse faults and in veins. *Quaternary Res.* **37**, 304–314.

Avigour, A., Magaritz, M., Issar, A., Dodson, M.H., 1990. Sr isotope study of vein and cave calcites from southern Israel. *Chem. Geol.* **82**, 69–81.

Avni, Y., 1997. *Geological evolution of the central Negev as an indicator of the evolution of the Dead Sea Transform western margin in the late Neogene and Quarternary*. PhD thesis, Hebrew University of Jerusalem, 240 pp. (in Hebrew with English Abstract).

Avni, Y., Bartov, Y., Garfunkel, Z., Ginat, H., 2001. The Arava Formation—A Pliocene sequence in the Arava Valley and its western Margin, southern Israel. *Isr. J. Earth Sci.* **50**, 101–120.

Avni, Y., Bartov, Y., Garfunkel, Z., Ginat, H., 2000. Evolution of the Paran drainage system and its relation to the Plio-Pleistocene history of the Arava Rift western margin, Israel. *Isr. J. Earth Sci.* **49**, 215–238.

Banner, J.L., 1995. Application of the trace element and isotope geochemistry of strontium to studies of carbonate diagenesis. *Sedimentology* **42**, 805–824.

Bartov, Y., 1974. *The faults and structural domes of central Sinai; structural and paleogeographic problems*. PhD thesis, Hebrew University of Jerusalem, 143 pp. (In Hebrew with English abstract).

Bartov, Y., Eyal, Y., Garfunkel, Z., Steinitz, G., 1972. Late Cretaceous and Tertiary stratigraphy and paleogeography of southern Israel. *Isr. J. Earth Sci.* **21**, 69–97.

Bentor, Y.K., 1952. Magmatic intrusions and lava-sheets in the Ramon area of the Negev (southern Israel). *Geol. Mag.* **89**, 129–140.

Bentor, Y.K., 1953. Origin of the mineral deposits of the Negev (southern Israel). Unpublished report.

Bentor, Y.K., Vroman, A., 1954. A structural contour map of Israel (1:250000) with remarks on its dynamical interpretation. *Bull. Res. Counc. Isr.* **2**.

Bethke, C.M., 1986. Hydrologic constrains on the genesis of the Upper Mississippi Valley mineral district from Illinois basin brines. *Econ. Geol.* **81**, 233–249.

Bethke, C.M., Marshak, S., 1990. Brine migrations across North America—the plate tectonics of groundwater. *Annu. Rev. Earth Planet. Sci.* **18**, 287–315.

Beyth, M., 1987. The Precambrian magmatic rocks of Timna Valley, southern Israel. *Precambrian Res.* **36**, 21–38.

Beyth, M., Reischman, T., 1996. The age of the quartz monzonite, the youngest plutonic intrusion in the Timna igneous complex. *Isr. J. Earth Sci.* **45**, 223–226.

Beyth, M., Stern, J.R., Altherr, R., Kroner, A., 1994. The Late Precambrian Timna igneous complex, southern Israel: evidence for comagmatic-type sanukitoid monzodiorite and alkali granite magma. *Lithos* **31**, 103–124.

Burke, W.H., Denison, R.E., Herthington, E.A., Koepnick, R.B., Nelson, H.F., Otto, J.B., 1982. Variations of sea water $^{87}Sr/^{86}Sr$ throughout Phanerozoic time. *Geology* **10**, 516–519.

DePaolo, D.J., 1986. Detailed record of the Neogene Sr isotopic evolution of seawater from DSDP site 590B. *Geology* **14**, 103–106.

Dessau, G., 1951. Report on the sulfur occurrence of Wadi Jirafi. *Isr. Geol. Surv.* Unpublished report.

Doron, Y., 2000. U-Th-Pb isotope system in rock veins along the Dead Sea Rift Valley, MSc thesis, The Hebrew University (in Hebrew).

Dvory, N.Z., 2002. *Subsurface study of the Paran and Thamad faults area*. M.Sc thesis, Hebrew University of Jerusalem, 82 p.

Faure, G., 1986. *Principles of Isotope Geology*. John Wiley.

Fleischer, E., Goldberg, M., Gat, J.R., Magaritz, M., 1977. Isotopic composition of formation waters from deep drillings in southern Israel. *Geochim. Cosmochim. Acta* **41**, 511–525.

Garfunkel, Z., 1999. History and paleogeography during the Pan-African orogen to stable platform transition. Reappraisal of the evidence from the Elat area and northern Arabian Shield. *Isr. J. Earth Sci.* **48**, 135–157.

Garfunkel, Z., 1988. Pre-Quaternary geology of Israel. In: Yom-Tov, Y., Tchernov, E. (Eds.), *The Zoogeography of Israel*. D. Junk, Dordrecht, pp. 7–34.

Garven, G., 1995. Continental-scale groundwater flow and geologic processes. *Ann. Rev. Earth Planet. Sci.* **23**, 89–117.

Garven, G., Ge, S., Person, M.A., Sverjensky, D.A., 1993. Genesis of stratabound ore deposits in the Midcontinent basins of North America; 1. The role of regional groundwater flow. *Am. J. Sci.* **293**, 497–568.

Ginat, H., Zilberman, E., Enzel, Y., 2000. Tectonic and paleogeographic significance of the Edom river, a Pliocene stream that crossed the Dead Sea Rift Valley. *Isr. J. Earth Sci.* **49**, 143–158.

Grosz, S., Matthews, A., Ilani, S., Ayalon, A., Garfunkel, Z., 2006. Iron mineralization and dolomitization in the Paran Fault zone, Israel: implications for low-temperature basinal fluis processes near the Dead Sea Transform. *Geofluids* **6**, 137–153.

Gvirtzman, Z., Bartov, Y., Garfunkel, Z., Rotstein, Y., 1994. Mesozoic magmatism in the central Negev (southern Israel): implications from magnetic anomalies. *Isr. J. Earth Sci.* **43**, 21–38.

Hanreck, R.G., 1952. Wadi Jirafi iron area. *Isr. Geol. Surv.* Unpublished report.

Harlavan, Y., Erel, Y., Blum, J.D., 1998. Systematic changes in lead isotopic composition with soil age in glacial granitic terrains. *Geochim. Cosmochim. Acta* **62**, 33–46.

Henig, S., 2004. Geochemical and isotopic (O, H, Se, B) characterization of Lower Cretaceous sandstone (Nubian) aquifer in the Negev and the Arava, Israel. MSc thesis, Ben Gurion University, Israel (in Hebrew).

Hess, J., Bender, M.L., Schilling, J.G., 1986. Evolution of the ratio of Strontium-87 to Strontium-86 in seawater from Cretaceous to present. *Science* **231**, 979–984.

Heyl, A.V., Delevaux, R.E., Zartman, R.E., Brock, M.R., 1966. Isotopic study of Galenas from the Upper Mississippi Valley, the Illinois-Kentucky, and some Appalachian valley mineral districts. *Econ. Geol.* **61**, 933–961.

Heyl, A.V., Landis, G.P., Zartman, R.E., 1974. Isotopic evidence for the origin of Mississippi valley-type mineral deposits: a review. *Econ. Geol.* **69**, 992–1006.

Ilani, S., 1989. Epigenetic metallic mineralization along tectonic elements in Israel. Ph.D. thesis, University of Tel Aviv, Israel (in Hebrew with English abstract).

Ilani, S., Kronfeld, J., Flexer, A., 1985. Iron-rich veins related to structural lineaments, and the search for base metals in Israel. *J. Geochem. Explor.* **24**, 197–206.

Ilani, S., Rosenthal, E., Kronfeld, J., Flexer, A., 1988. Epigenetic dolomitization and iron mineralization along faults and their possible relation to the paleohydrology of southern Israel. *Appl. Geochem.* **3**, 487–498.

Issar, A., Bein, A., Michaeli, A., 1972. On ancient water of the Upper Nubian sandstone aquifer in central Sinai and southern Israel. *J. Hydrol.* **17**, 353–374.

Jahn, B., Simonson, B.M., 1995. Carbonate Pb–Pb ages of the Wittenoom Formation and Carawine Dolomite, Hamersley Basin, Western Australia (with implications to their correlation with the Transvaal Dolomite of South Africa). *Precambrian Res.* **72**, 247–261.

Lang, B., Hebeda, E.H., Priem, H., Steinitz, G., Verdurmen, A.Th., 1988. K–Ar and Rb–Sr ages of Early Cretaceous magmatic rocks from Makhtesh Ramon, southern Israel. *Isr. J. Earth Sci.* **37**, 65–72.

Leach, D., Bradley, D., Lewchuk, M.T., Symons, D.T.A., deMarsily, G., Brannon, J., 2001. Mississippi valley-type lead–zinc deposits through geologic time: implications from recent age-dating research. *Miner. Deposita* **36**, 711–740.

Levite, D., 1966. Magmatic phenomena in the Arava, Israel. Msc thesis, The Hebrew University, Israel (in Hebrew).

Listovsky, N., 2004. Geochemical evolution of metalliferous fluids along the Paran Tectonic line (Menuha Ridge, southern Israel). M.Sc thesis, Hebrew University of Jerusalem, 82 p.

Moorbath, S., Taylor, P.N., Orpen, J.L., Treloar, P., Wilson, J.F., 1987. First direct radiometric dating of Archean stromatolitic limestone. *Nature* **326**, 865–867.

Ohle, E.L., 1980. Some considerations in determining the origin of ore deposits of the Mississippi Valley type. *Econ. Geol.* **75**, 161–172.

Robb, L., 2005. *Introduction to Ore-Forming Processes*. Blackwell Publishing, Oxford UK, pp. 373.

Sakal, E., 1998. Geology of the Menuha Ridge. *Geol. Surv. Isr. Rep.* **GSI/14/98**, 115 pp. (in Hebrew with English abstract).

Segev, A., Goldshmidt, V., Rybakov, M., 1999. Late Precambrian–Cambrian tectonic setting of the crystalline basement in the northern Arabian–Nubian Shield as derived from gravity and magnetic data: Basin and range characteristics. *Isr. J. Earth Sci.* **48**, 159–178.

Shraga, G.M., 1971. The hydrothermal iron deposits of the Menuha Ridge. *Isr. J. Earth Sci.* **20**, 51–88.

Sneh, A., Bartov, Y., Rosensaft, M., 1998. Geological Map of Israel, 1:200,000, Sheet 4. The Geological Survey of Israel, Jerusalem.

Solomonica, S., 1952. *Short Report on a Visit to the Iron Ore in Wadi Jerafi*. Makhteshim, Hakirya, Israel.

Stanislavsky, E., Gvirtzman, H., 1999. Basin-scale migration of continental-rift brines: paleohydrologic modeling of the Dead Sea basin. *Geology* **27**, 791–794.

Starinsky, A., 1974. Relation between Ca-chloride brines and sedimentary rocks in Israel. Ph.D. thesis, Hebrew University, Jerusalem (in Hebrew, English abstr).

Steefel, C.I., Van Cappellen, P.C., 1998. Reactive transport modeling of natural systems. *J. Hydrology* **209**, 1–7.

Stein, M., Starinsky, A., Katz, A., Goldstein, S.L., Machlus, M., Schramm, A., 1997. Strontium isotopic, chemical, and sedimentological evidence for the evolution of Lake Lisan and the Dead Sea. *Geochim. Cosmochim. Acta* **61** (18), 3975–3992.

Stein, M., Starinsky, A., Agnon, A., Katz, A., Raab, M., Spiro, B., Zak, I., 2000. The impact of brine-rock interaction during marine evaporite formation on the isotopic Sr record in the oceans: evidence from Mt. Sedom, Israel. *Geochim. Cosmochim. Acta* **64** (12), 2039–2053.

Stein, M., Agnon, A., Katz, A., Starinsky, A., 2002. Strontium isotopes in discordant dolomite bodies of the Judea Group, Dead Sea basin. *Isr. J. Earth Sci.* **51** (3–4), 219–224.

Steinitz, G., Bartov, Y., 1991. The Miocene–Pliocene history of the Dead Sea segment of the Rift in the light K–Ar ages of basalts. *Isr. J. Earth. Sci.* **40**, 199–208.

Sverjensky, D.A., 1986. Genesis of Mississippi valley-type lead–zinc deposits. *Ann. Rev. Earth Planet. Sci.* **14**, 177–199.

Weissbrod, T., Nachmias, J., 1986. Stratigraphic significance of heavy minerals in the late Precambrian–Mesozoic clastic sequence (''Nubian sandstone'') in the near east. *Sedimentary Geol.* **47**, 263–291.

Whitfield, M., Turner, D.R., 1987. The role of particles in regulating the composition of sea water. In: Stumm, W. (Ed.), *Aquatic Surface Chemistry*. John Wiley, pp. 457–493.